INSTITUT NATIONAL DE RECHERCHE EN INFORMATIQUE ET EN AUTOMATIQUE

Deterministic and Probabilistic Q-Ball Tractography: from Diffusion to Sharp Fiber Distributions

Maxime Descoteaux — Rachid Deriche — Alfred Anwander

N° 6273

August 2007

Thème BIO

ISSN 0249-6399

Deterministic and Probabilistic Q-Ball Tractography: from Diffusion to Sharp Fiber Distributions

Maxime Descoteaux* , Rachid Deriche† , Alfred Anwander‡

Thème BIO —Systèmes biologiques
Projet Odyssée

Rapport de recherche n° 6273 —August 2007 — 36 pages

Abstract: We propose a deterministic and a probabilistic extension of classical diffusion tensor imaging (DTI) tractography algorithms based on a sharp fiber orientation distribution function (ODF) reconstruction from Q-Ball Imaging (QBI). An important contribution of the paper is the integration of some of the latest state-of-the-art high angular resolution diffusion imaging (HARDI) data processing methods to obtain accurate and convincing results of complex fiber bundles with crossing, fanning and branching configurations. First, we develop a new deconvolution *sharpening* transformation from diffusion ODF (dODF) to fiber ODF (fODF). We show that this sharpening transformation improves angular resolution and fiber detection of QBI and thus greatly improves tractography results. The angular resolution of QBI is in fact improved by approximately 20° and the fODF is shown to behave very similarly of the fiber orientation density (FOD) estimated from the spherical deconvolution method of Tournier et al. Another major contribution of the paper is the extensive comparison study on human brain datasets of our new deterministic and probabilistic tracking algorithms. As an application, we show how the reconstruction of transcallosal fiber connections intersecting with the corona radiata and the superior longitudinal fasciculus can be improved with the fODF in a group of 8 subjects. Current DTI based methods neglect these fibers, which might lead to wrong interpretations of the brain functions.

Key-words: fiber tractography, diffusion tensor imaging (DTI), high angular resolution diffusion imaging (HARDI), q-ball imaging (QBI), spherical deconvolution (SD), orientation distribution function (ODF)

* Maxime.Descoteaux@sophia.inria.fr
† Rachid.Deriche@sophia.inria.fr
‡ anwander@cbs.mpg.de. Max Planck Institute for Human Cognitive and Brain Science, Leipzig, Germany

Déconvolution Sphérique de l'ODF et Tractographie Déterministe et Probabiliste en Imagerie par Q-Ball

Résumé : Nous proposons d'étendre les algorithmes de tractographie classiques développés sur les images de tenseur de diffusion (DTI) pour les appliquer à l'imagerie par Q-Ball (QBI). Une contribution importante de ce rapport est l'intégration de l'état de l'art des méthodes de traitement d'images de diffusion à haute résolution angulaire (HARDI) pour obtenir des réseaux complexes de l'architecture neuronale de la matière blanche comportant des croisements, des embranchements et des configurations en éventail. D'abord, nous développons une nouvelle méthode de déconvolution sphérique pour transformer la fonction de distribution de diffusion des orientations (dODF) en une fonction de distribution d'orientations des fibres (fODF). Cette transformation de *sharpening* augmente la résolution angulaire d'environ 20° et facilite l'extraction des maxima de l'ODF. Par conséquent les résultats de tractographie sur les fODFs sont plus complets et de meilleure qualité. Ensuite, nous démontrons que la fODF et la distribution obtenue par déconvolution sphérique classique de Tournier et al se comportent de la même manière sur des simulations de données HARDI. Enfin, une autre contribution importante du rapport est l'étude poussée et la comparaison des algorithmes de tractographie déterministes et probabilistes sur des données HARDI réelles à partir du DTI, de la dODF et de la fODF. Nous montrons une application intéressante sur le corps calleux et la reconstruction des fibres transcallosales. Ces fibres sont normalement complétement ignorées par les techniques de tractographie en DTI car elles croisent le faisceau supérieur longitudinal ainsi que la couronne rayonnante. Notre tractographie en QBI basée sur la fODF nous permet de retrouver ces fibres transcallosales sur une base de données de 8 sujets, ce qui nous permet une connaissance anatomique plus fine de ces parties du cerveau.

Mots-clés : Tractographie, imagerie du tenseur de diffusion (DTI), imagerie de diffusion à haute résolution angulaire (HARDI), imagerie par Q-ball (QBI), function de distribution des orientations (ODF), déconvolution sphérique

Contents

1 Introduction

Diffusion magnetic resonance imaging (MRI) *tractography* is the only non-invasive tool to obtain information on the neural architecture in vivo of the human brain white matter. Tractography is needed to understand functional coupling between cortical regions of the brain and is important for characterization of neuro-degenerative diseases, for surgical planning and for many other medical applications [42]. Currently, white matter fiber tractography is most commonly implemented using the principal diffusion direction of the diffusion tensor (DT) data. The diffusion tensor (DT) model [6] characterizes the orientation dependence of the diffusion probability density function (pdf) of the water molecule. An important limitation of the DT model is the Gaussian diffusion assumption, which implies that there can only be a single fiber population per voxel. At the resolution of DTI acquisitions, this is an important problem since it is known that many voxels have low anisotropy index due to non-Gaussian diffusion coming from multiple fibers crossing, branching, fanning or in a bottleneck. In fact, the resolution of DTI acquisitions is usually between 3 mm^3 and 15 mm^3, while the diameter of bundles of axons considered in fiber tractography are on the order of 1mm and individual physical fibers on the order of 1-30 μm [42]. Thus, tractography algorithms based on the DT can follow false tracts due to diffusion profiles that are prolate or can prematurely stop in regions of isotropic tensors.

To overcome these limitations of the DT, new higher resolution acquisition techniques such as Diffusion Spectrum Imaging (DSI) [57], High Angular Resolution Diffusion Imaging (HARDI) [57], Q-Ball Imaging (QBI) [58] and composite hindered and restricted model of diffusion (CHARMED) [5] have been proposed to estimate the Orientation Distribution Function (ODF) [58] of water molecules. Moreover, other HARDI reconstruction techniques have been proposed to estimate high order spherical functions such as the Persistent Angular Structure (PAS) [30], the Fiber Orientation Density (FOD) [1, 3, 14, 55, 56], the Diffusion Orientation Transform (DOT) [43] and multi-tensor distributions [40, 57]. All these HARDI techniques are developed to deal with non-Gaussian diffusion process and reconstruct spherical functions with potentially multiple maxima aligned with the underlying fiber populations. A good review of all these high order reconstruction techniques can be found in [2, 16].

Hence, one naturally wants to generalize existing DT-based tractography algorithms with HARDI-based techniques to better deal with fiber crossings. In tractography, two families of algorithms exist: deterministic and probabilistic algorithms. Research groups have recently started to generalize both deterministic and probabilistic DT-based tracking algorithms to use some of the HARDI reconstruction methods mentioned above. Popular high order functions used in the literature are the ODF [10, 11, 24, 46, 57], the PAS function [44] and variants of multi-tensor fitting models [8, 23, 36, 49]. The latter techniques show improvement in tracking results where the DT model fits the data poorly and show preliminary fiber bundles with some crossing and branching configurations handled. In this paper, the high order spherical function used is the ODF estimated from QBI because it is model-free and it can be computed analytically, robustly and quickly with our new approach proposed in [18]. The ODF is the basis of our new tracking algorithms.

To illustrate the contributions of our new tracking algorithms, we focus on complex fiber bundles such as projections of callosal fibers to the cortex. These bundles have been studied extensively

in the neuroanatomical and DTI literature (e.g. [28]). The corpus callosum (CC) is involved in the interhemispheric interaction of cortical regions and the reconstruction of fibers connecting the cerebral hemispheres is of major interest for cognitive research and clinical praxis. While DT-based tractography finds fibers passing through the CC connected with the medial/dorsal cortex, lateral and ventral fibers are not found, since these fibers cross the corona radiata and the superior longitudinal fasciculus (SLF). Only a recent study [48] proposed to use a HARDI-based method to reconstruct fibers of the genu and splenium of the CC.

The goal of the paper is thus to integrate the full multidirectional information of a sharp q-ball fiber ODF in both a new deterministic and a new probabilistic tractography algorithm with emphasis on a comparison on real human brain fiber bundles where classical deterministic and probabilistic DT techniques fail. The contributions of the paper are threefold: 1) We first develop a new transformation from diffusion ODF (dODF) to *sharp fiber* ODF (fODF). We show that this transformation improves angular resolution and fiber detection of QBI. 2) We then extensively validate and compare the fODF against the classical FOD estimated from spherical deconvolution [55] on simulations and find similar behaviors between both methods. 3) We last propose a new deterministic and probabilistic tractography algorithm using all the multidirectional information of the sharp fiber ODF. We perform a comparison study of both tracking algorithms on complex fiber bundles of the cerebral anatomy In particular, we investigate how the reconstruction of transcallosal fiber connections can be improved by the sharp fiber ODF in voxels where fibers cross the corpus callosum. We show, on 8 subjects, areas of the corpus callosum where the new probabilistic tracking finds fibers connecting the ventral and lateral parts of the cortex, fibers currently missed when using DT-based algorithms.

The paper is outlined as follows. In Section 2, we review relevant tractography background literature to illustrate and motivate our new deterministic and probabilistic algorithms. We then review our fast, regularized and analytical ODF estimation [18] in Section 3.1 and develop the deconvolution sharpening transformation that produces the sharp fiber ODF in Section 3.2. The deterministic and probabilistic tractography algorithms are developed in Sections 3.3 and 3.4 respectively. We next present qualitative and quantitative evaluations of the deconvolution sharpening and compare the deterministic and probabilistic tractography algorithms on several complex fiber bundles in Section 4. Finally, we conclude with a discussion of the results and present directions for future work in Section 5.

2 Tractography Overview

The most intuitive tracking algorithms are the classical deterministic streamline (STR) tracking algorithms [7, 13, 41] and slightly more complex tensor deflection (TEND) algorithms [38, 59] used in many applications [29]. Many other DT-based streamlines and flow-based approaches also exist. A good review and discussion of DT-based algorithms can be found in [42]. Here, we focus on HARDI-based tractography algorithms.

Recently, [24, 57] have proposed a generalized streamline tracking algorithm based on the principal direction of the diffusion ODF computed from DSI. In [36], a multi-tensor local model of the data is used to extend the fiber assignment by continuous tracking (FACT) [41] algorithm. Moreover, to deal with more complex fiber configurations, [45] extended streamline tracking with a mixture of

Gaussian densities and similarly, [23] recently extended the TEND model with a bi-Gaussian model. Finally, based on the classical diffusion ODF reconstructed from QBI [58] and the very recent regularized version of the diffusion ODF [51], [10] proposes a streamline approach with curvature constraint following all maxima to deal with fibers crossing. In this paper, we propose another extension to streamline tractography based on the full multidirectional information of the sharp fiber ODF. From this sharp fiber ODF, we extract all available maxima and allow for splitting in multiple directions at each step. Not only can the tracking propagate through fiber crossings but it can also deal with fibers fanning and branching.

Existing deterministic HARDI-based techniques mostly show that tracking is improved where the DT model fits the data poorly. However, these deterministic tractography algorithms inherit the classical limitations of deterministic algorithms such as choice of initialization, sensitivity in estimated principal direction and lack of straightforward way to compute statistics on tracts and lack of connectivity information between regions of the brain. To overcome limitations of deterministic tractography, DT-based probabilistic algorithms have been used such as [9, 21, 37, 45, 49]. This also motivates the development of new HARDI-based probabilistic algorithms. Probabilistic algorithms are computationally more expensive than deterministic algorithms but can better deal with partial volume averaging effects and noise uncertainty in underlying fiber direction. Most importantly, the output of the algorithms are usually designed to give a connectivity index measuring how probable two voxels are connected to one another.

HARDI-based probabilistic tractography have recently been published in the literature [8, 44, 46] to generalize several existing DT-based methods. First, in [8] a mixture of Gaussian model is used to extend the probabilistic Bayesian DT-based tracking [9]. In [46], Monte Carlo particles move inside the continuous field of q-ball diffusion ODF and are subject to a trajectory regularization scheme. In [44], an extension to their DT-based approach [45] is also proposed using a Monte Carlo estimation of the white matter geometry. Their implementation is based on PASMRI with a new noise modeling component. Overall, these methods show successful tracking of several fiber bundles difficult to recover with DT-based techniques. The methods have mainly focused on fibers with crossing configurations and have not attempted to account for fibers demonstrating high curvature or points where fiber populations branch or fan. In this paper, our new probabilistic algorithm attempts to account for branching and fanning fiber populations as well as fibers crossing.

Normally, an advantage of the probabilistic tractography techniques is that they are based on the full spherical function considered (DT, ODF, PAS, etc...) and not only on the principal direction or maximum(a) extracted. However, this creates a problem when the spherical function profiles are smooth and have significant isotropic parts. In that case, tractography produces diffusive tracking results that leak into unexpected regions of the white matter. This is a well-known problem in probabilistic DT tractography and has not been thoroughly studied in the literature. Typically, one simply take a power of the diffusion tensor [4, 35, 38, 54] to increase the ratio of largest to smallest eigenvalue and thus have enhanced and more elongated tensors. However, this heuristic transformation can create degenerate tensors with second and/or third null eigenvalue.

To solve this problem of diffusive tracking and leaking in ODF-based tracking methods, one needs to use the fiber ODF to obtain more complete and accurate tracts. The relation between diffusion ODF and fiber ODF is unknown and is currently an open problem in the field [46, 57].

Spherical deconvolution (SD) methods [1, 3, 14, 55] reconstruct such a fiber orientation distribution, the FOD, without the need of the diffusion ODF. However, anybody working with QBI and diffusion ODFs has the problem of dealing with smooth ODFs that have a large diffusion part not aligned with the principal fiber directions. Hence, we propose a new ODF sharpening deconvolution operation which has the desired effect of transforming the diffusion ODF into a sharp fiber ODF and we extensively compare our sharp fiber ODF with the classical FOD estimated from SD [55]. We show that this ODF deconvolution transformation is a natural pre-processing task when one is interested in fiber tracking.

3 Methods

In this section, we introduce our analytical solution to QBI developed in [18], our sharpening deconvolution operation transforming the diffusion ODF into a sharp fiber ODF and our new deterministic and probabilistic tracking algorithms.

3.1 Analytical Regularized ODF from QBI

Tuch [57, 58] showed that the ODF could be estimated directly from the raw HARDI measurements on a single sphere by a numerical implementation of the Funk-Radon transform (FRT). We have showed in [18] that this FRT could be solved analytically, robustly, and more quickly. The key idea is to express the HARDI signal as a spherical harmonic (SH) series of order ℓ and to solve the FRT using the Funk-Hecke theorem. Note that Anderson [3] and Hess et al [26] have recently developed independently a similar analytical solution for the ODF reconstruction in QBI. Despite the fact that our analytical solution is similar, our regularized estimation part, the derivation, the experimental results, and the validation phase are quite different and clearly demonstrated in [18].

In our analytical QBI solution, the signal at position p is first estimated as

$$S(\mathbf{u})_p = \sum_{j=1}^{R} c_j Y_j(\mathbf{u}), \tag{1}$$

where $S(\mathbf{u})$ is the measured diffusion weighted signal in each of the N gradient direction $\mathbf{u} := (\theta, \phi)$ on the sphere (θ, ϕ obey physics convention, $\theta \in [0, \pi], \phi \in [0, 2\pi]$), c_j are the SH coefficients describing the signal, Y_j is the j^{th} element of the SH basis and $R = (1/2)(\ell + 1)(\ell + 2)$ is the number of terms in the basis of order ℓ when choosing only even orders. Our implementation is based on a modified symmetric, real, orthonormal basis and the coefficients c_j are obtained with a Laplace-Beltrami regularization least-square approach to eliminate unnecessary higher order terms in the SH approximation [17]. Note that this kind of regularization was also applied with success to the FOD estimated with spherical deconvolution in [50] using a gradient constraint instead of a Laplace-Beltrami constraint. The exact Laplace-Beltrami regularized expression for the coefficients c_j is given in [17, Eq.15]. Our Laplace-Beltrami regularization is using the right operator for the space of functions of the unit sphere and gives better estimation and more robust fiber detection [18] than without regularization [3] or with classical Tikhonov regularization [26].

Spherical harmonics allow the simplification of the Funk-Radon Transform (FRT) by the Funk-Hecke theorem. The final ODF reconstruction, Ψ, at position p, is simply a diagonal linear transformation of the signal SH coefficients c_j,

$$\Psi(\mathbf{u})_p = \sum_{j=1}^{R} 2\pi P_{\ell_j}(0) c_j Y_j(\mathbf{u}), \tag{2}$$

where ℓ_j is the order associated with j^{th} SH basis element (for $j = \{1, 2, 3, 4, 5, 6, 7, ...\}$, $\ell_j = \{0, 2, 2, 2, 2, 2, 4, ...\}$) and $P_{\ell_j}(0)$ a Legendre polynomial with simple expression since we use only even orders in the SH basis,

$$P_{\ell_j}(0) = (-1)^{\ell_j/2} \left(\frac{3 \cdot 5 \cdots (\ell_j - 1)}{2 \cdot 4 \cdots \ell_j} \right). \tag{3}$$

3.2 Sharpening and the Fiber ODF

Anybody working with QBI and/or a diffusion ODF has the problem of dealing with a smooth ODF that has a large diffusion part not aligned with the principal fiber directions. The relation between diffusion ODF and fiber ODF is unknown and is currently an open problem in the field [46, 57]. Here, we describe the sharpening operation that aims to transform this smooth diffusion ODF into a sharp fiber ODF [19].

The sharpening operation is a simple linear transformation of the spherical harmonic (SH) coefficients describing the diffusion ODF. The idea is to use spherical deconvolution. Our approach is inspired by the original spherical deconvolution approach proposed by Tournier et al [55], where the measured signal is expressed as the convolution on the unit sphere of the fiber response function with the fiber orientation density function (FOD) [55, Fig.1]. Assuming a particular fiber response function representing the diffusion signal attenuation that would be measured for a single fiber, [55] shows that the deconvolution of the signal with the response function gives the FOD. This was also recently used by others in [14, 56].

Here, the starting point is not the measured signal but our estimated diffusion ODF described in the previous Section 3.1. We want to deconvolve the estimated smooth diffusion ODF by a certain diffusion ODF kernel for a single fiber in order to obtain a sharpened ODF. The procedure is sketched in Fig. 1. We assume that the estimated diffusion ODF, Ψ, is formed by convolution between the single fiber diffusion ODF kernel, R, and the true fiber FOD. Hence, the deconvolution of the diffusion ODF by the diffusion ODF kernel can recover a sharp fiber ODF.

The convolution on the sphere between R and Ψ_{sharp} (Fig. 1a) can be written as

$$\Psi(\mathbf{u}) = \int_{|\mathbf{w}|=1} R(\mathbf{u} \cdot \mathbf{w}) \Psi_{\text{sharp}}(\mathbf{w}) d\mathbf{w}. \tag{4}$$

In order to solve this integral, we first replace Ψ and Ψ_{sharp} with their respective SH estimation of order ℓ, $\sum_j c_j Y_j(\mathbf{u})$ and $\sum_j c_{j_{\text{sharp}}} Y_j(\mathbf{u})$ and obtain

$$\sum_{j=1}^{R} c_j Y_j(\mathbf{u}) = \sum_{j=1}^{R} c_{j_{\text{sharp}}} \int_{|\mathbf{w}|=1} R(\mathbf{u}\cdot\mathbf{w}) Y_j(\mathbf{w}) d\mathbf{w}.$$

At this point, we use the Funk-Hecke theorem stated in Appendix A to solve the integral over the sphere between R and the spherical harmonic Y_j. The Funk-Hecke formula is a theorem that relates the inner product of any spherical harmonic with any continuous function defined on the interval $[-1, 1]$. It was also at the core of our analytical ODF estimation presented in Section 3.1 [18]. Hence, we obtain

$$c_{j_{\text{sharp}}} = \frac{c_j}{f_j}, \qquad \text{where} \qquad f_j = 2\pi \int_{-1}^{1} P_{\ell_j}(t) R(t) dt, \tag{5}$$

P_{ℓ_j} is a Legendre polynomial of order ℓ_j and coefficients f_j come from the Funk-Hecke formula, which is expanded in Eq. 15 of Appendix B. Therefore, the final sharp fiber ODF expression at position p is given by

$$\Psi_{\text{sharp}}(\mathbf{u})_p = \sum_{j=1}^{R} 2\pi P_{\ell_j}(0) \frac{c_j}{f_j} Y_j(\mathbf{u}). \tag{6}$$

For the rest of the paper, we define this ODF as the sharp fiber ODF (fODF).

The main consideration is thus the creation of a viable diffusion ODF kernel R. Assuming that a Gaussian can describe the diffusion of water molecules for a single fiber, we choose a prolate tensor profile with eigenvalues $e_1 \geq e_2 = e_3$ to represent this Gaussian. Then, using the analytical relation between diffusion tensor and diffusion ODF [18, 58], we obtain our diffusion ODF kernel R. In the synthetic simulations of [18, 55] and in the model-based approach of [14], values of $[e_2, e_2, e_1]$ are chosen from physiological data. Here, we prefer to estimate the diffusion ODF kernel directly from our real dataset, as done in Tournier et al [55, 56] for single fiber response function. All details are given in Appendix B, where the analytical diffusion ODF kernel, R, is derived. In practice, the average prolate tensor profile is estimated from 300 voxels with highest FA value, as these tensors can each be assumed to contain a single fiber population.

3.3 Deterministic Multidirectional ODF Tracking

We extend the classical streamline techniques [7, 13, 42] based on diffusion tensor principal direction to take into account multiple ODF maxima at each step. We denote $p(s)$ as the curve parameterized by its arc-length. This curve can be computed as a 3D path adapting its tangent orientation locally according to vector field $\mathbf{v}$. Hence, for a given starting point p_0, we solve $p(t) = p_0 + \int_0^t \mathbf{v}(p(s))ds$. The integration is typically performed numerically with Euler or Runge-Kutta schemes of order 2 or 4. In the Euler case, we have the discrete evolution equation

$$p_{n+1} = p_n + \mathbf{v}(p_n)\Delta s, \tag{7}$$

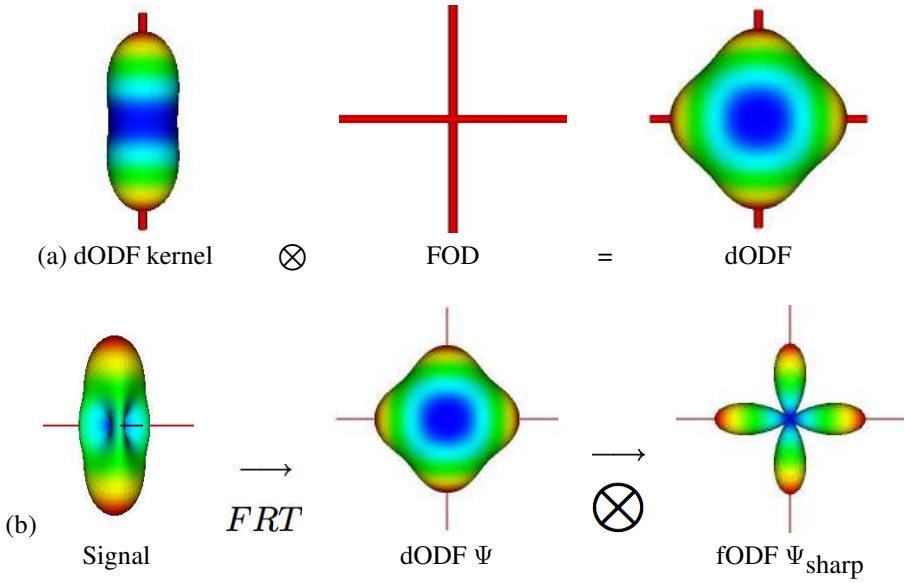

Figure 1: Sketch of the convolution/deconvolution. In (a), the convolution between the diffusion ODF (dODF) kernel and the fiber orientation function (FOD) produces a smooth diffusion ODF. In (b), we show a sketch of the deconvolution sharpening. The Funk-Radon Transform (FRT) of the simulated HARDI signal on the sphere produces a smooth diffusion ODF. This diffusion ODF is transformed into a sharp fiber ODF (fODF) by the deconvolution with the diffusion ODF kernel of (a).

where Δs is a small enough step size to obtain subvoxel precision. A continuous linear, cubic, spline or geodesic [39] interpolation of the vector field can be done at each step for the subvoxel points. A good review is found in [42] and more recently in [11, 25].

For seed point p_0, for a given anisotropy measure A that can be FA, Generalized FA (GFA) [58] or any other measure, for anisotropy threshold t_{aniso}, for curvature threshold t_θ, for ExtractMax(Ψ, p) a function returning the list l of vector(s) oriented along each ODF, Ψ, maximum(a) at point p, for size(l) returning the size of list l and for l_j representing the j^{th} element of list l, our algorithm can be described as follows:

(0) Estimate field of fODF, Ψ_{sharp}, with Eq. 6
(1) **Set** seed p_0 and **set** $\mathbf{v}(p_0) = \text{argmax}_{\mathbf{u}} \Psi_{\text{sharp}}(\mathbf{u})_{p_0}$
(2) Update curve according to Eq. 7.
If $A(p_n) < t_{aniso}$ **then** STOP;
If $\dfrac{\mathbf{v}(p_n) \cdot \mathbf{v}(p_{n-1})}{||\mathbf{v}(p_n)||||\mathbf{v}(\mathbf{p_{n-1}})||} > t_\theta$ **then** STOP;
Let $l = \text{ExtractMax}(\Psi_{\text{sharp}}, p_n)$. **If** size$(l) > 1$
then SPLIT curve; **for** $i = 1$ to $|l|$
do (1) with $p_0 = p_n$ and $\mathbf{v}(p_0) = l_i$;

ODF estimation is done with order $\ell = 4, 6$ or 8 as in [18] and ODF kernel estimated from our real dataset. To extract ODF maxima, it is generally assumed that they are simply given by the local maxima of the normalized ODF ([0,1]), where the function surpasses a certain threshold (here, we use 0.5). In practice, we project the ODF onto the sphere tessellated with a fine mesh. We use a 16th order tessellation of the icosahedron, which gives 1281 sample directions on the sphere. Then, we implement a finite difference method on the mesh. If a mesh point is above all its neighbors and if this point has an ODF value above 0.5, we keep the mesh point direction as a maxima. This thresholding avoids selecting small peaks that may appear due to noise. Other more complex methods exist to extract the maxima such the method presented in [27] or spherical Newton's method [55].

In our implementation, we use FA and $t_{aniso} = 0.1$ as a mask to prevent tracks to leak outside white matter, we set curving angle threshold $t_\theta = 75^\circ$ and $\Delta s = 0.1$ and we use Euler integration and classical trilinear interpolation to obtain dODF, fODF and DT at subvoxel precision. For the rest of the paper, DT-STR refers to this algorithm using the DT principal eigenvector, dODF-STR and fODF-STR refers to this algorithm using a single dODF/fODF maxima that is the closest to the incoming tangent direction of the curve, and SPLIT-STR refers to this algorithm using all available fODF maxima with splitting at each step.

3.4 Probabilistic fiber ODF Tracking

In this section, we propose an extension of the random walk method proposed by Anwander et al. [4] and Koch et al. [35] to use the multidirectional fiber ODF. Imagine a particle in a seed voxel moving in a random manner with a constant speed within the brain white matter. The transition probability to a neighboring point depends on the local fODF, Ψ_{sharp}. This fODF is discretized into 120 directions evenly distributed and at every time step, one of these 120 direction is picked at random according to the fODF distribution. This yields higher transitional probabilities along the main fiber directions. Hence, the particle will move with a higher probability along a fiber direction than perpendicular to it. We start a large number of particles from the same seed point, let the particles move randomly according to the local fODF and count the number of times a voxel is reached by the path of a particle. The random walk is stopped when the particle leaves the white matter volume.

For each elementary transition of the particle, the probability for a movement from the seed point x to the target point y in one of the 120 directions $\mathbf{u}_{xy}$ is computed as the product of the local fODFs in direction $\mathbf{u}_{xy}$, i.e.

$$P(x \to y) = \Psi_{\text{sharp}}(\mathbf{u}_{xy})_x \cdot \Psi_{\text{sharp}}(\mathbf{u}_{xy})_y \tag{8}$$

where $P(x \rightarrow y)$ is the probability for a transition from point x to point y and $\Psi_{\text{sharp}}(\mathbf{u}_{xy})_x$ is the fiber ODF in point x in direction y.

The transition directions in the local model are limited to 120 discrete directions corresponding to the angular sampling resolution of the acquired data, and the step size of the particle step was fixed to 0.5. We used trilinear interpolation of the fODF for the subvoxel position and projected to 120 discrete directions (same as our real data gradient encodings). Moreover, voxels within the CSF and voxels containing mainly gray matter were excluded from the tracking using a mask computed from a minimum FA value of 0.1 and a maximum ADC value of 0.0015. These values were optimized to produce a good agreement with the white matter mask from the T1 anatomy. The mask was morphologically checked for holes in regions of low anisotropy due to crossing fibers. Finally, a total of 100000 particles were tested for each seed voxel. To remove artifacts of the random walk, only voxels which were reached by at least 100 particles were used for further processing. For visualization purposes, the dynamic range of the connectivity values was changed by logarithmic transformation and the entire tractogram was normalized between 0 and 1. For the rest of the paper, the 3-dimensional distribution of connected voxels to the seed voxel is called a *tractogram*.

The main novelties in the probabilistic algorithm compared to previous published versions [4, 35] are the use of the fODF after deconvolution of the diffusion data, the higher angular sampling combined with a continuous interpolation of the data and the subvoxel tracking of the streamline. The deconvolution sharpening pre-processing step is shown to have a dramatic impact on the quality of the tractogram. For the rest of the paper, the method just described is referred to as fODF-PROBA.

3.5 Data Acquisition

3.5.1 Synthetic Data Generation

We generate synthetic ODF data using the multi-tensor model which is simple and leads to an analytical expression of the ODF [18]. For a given b-factor and noise level, we generate the diffusion-weighted signal

$$S(\mathbf{u}_i) = \sum_{k=1}^{n} p_k e^{-b\mathbf{u}_i^{\mathrm{T}} \mathbf{D_k} \mathbf{u}_i} + noise, \tag{9}$$

where $\mathbf{u}_i$ is the ith gradient direction on the sphere, n is the number of fibers, p_k is the volume fraction of the k^{th} fiber and $\mathbf{D_k}$ the k^{th} diffusion tensor profile oriented randomly. We use tensor profile $\mathbf{D}_k$ estimated directly on our real dataset using 300 voxels with highest FA from our real dataset. Finally, we add complex Gaussian noise with standard deviation of σ, producing a signal with signal to noise ratio (SNR) of $1/\sigma$.

3.5.2 Human Brain Data

Diffusion weighted data and high-resolution T_1-weighted images were acquired in 8 healthy right-handed volunteers (25 $\pm$ 4 years, 4 females) on a whole-body 3 Tesla Magnetom Trio scanner (Siemens, Erlangen) equipped with an 8-channel head array coil [4]. Written informed consent was obtained from all subjects in accordance with the ethical approval from the University of Leipzig.

The spin-echo echo-planar-imaging sequence, TE = 100 ms, TR = 12 s, 128 x 128 image matrix, FOV = 220 x 220 mm^2, consists of 60 diffusion encoding gradients [32] with a b-value of 1000 s/mm^2. Seven images without any diffusion weightings are placed at the beginning of the sequence and after each block of 10 diffusion weighted images as anatomical reference for offline motion correction. The measurement of 72 slices with 1.7mm thickness (no gap) covered the whole brain. Random variations in the data were reduced by averaging 3 acquisitions, resulting in an acquisition time of about 45 minutes. No cardiac gating was employed to limit the acquisition time. The issue of cardiac gating is discussed in [33]. Additionally, fat saturation was employed and we used 6/8 partial Fourier imaging, a Hanning window filtering and parallel acquisition (generalized auto-calibrating partially parallel acquisitions, reduction factor = 2) in the axial plane.

The brain is peeled from the T1-anatomy, which was aligned with the Talairach stereotactical coordinate system [53]. The 21 images without diffusion weightings distributed within the whole sequence were used to estimate motion correction parameters using rigid-body transformations [31], implemented in [22]. The motion correction for the 180 diffusion-weighted images was combined with a global registration to the T1 anatomy computed with the same method. The gradient direction for each volume was corrected using the rotation parameters. The registered images were interpolated to the new reference frame with an isotropic voxel resolution of 1.72 mm and the 3 corresponding acquisitions and gradient directions were averaged.

3.6 Evaluation of the Deconvolution Sharpening Transformation

3.6.1 Spherical Deconvolution

For comparison with our sharp fODF, we also reconstruct the FOD using spherical deconvolution [55]. We implement the filtered SD (fSD) [55] using spherical harmonics and low-pass filter [1,1,1,0.8,0.1] multiplying each coefficient of order $\ell \in \{0, 2, 4, 6, 8\}$ respectively (details in [56]. This filtering is introduced to reduce the effect of noise and spurious peaks problem produced by high order spherical harmonic coefficients of the FOD estimation. There are more very recent versions of spherical deconvolution with regularization [50] and positivity constraint with super-resolution [56] that have just appeared in the literature. Here, we choose to compare against the classical fSD [55] because it has been extensively studied in the literature.

3.6.2 Synthetic Data Experiment

We evaluate and quantify the angular resolution limitation, the fiber detection success and angular error made on the detected maxima when using the diffusion ODF (dODF) (Eq. 2), the sharp fiber ODF (fODF) (Eq. 6) and the filtered SD (fSD) [55] described in Section 3.6.1. First, to evaluate angular resolution limitations, we generate noise-free synthetic data for two fibers where we vary the crossing angle between fibers to determine the critical angle at which only a single maximum is detected instead of two. Then, to evaluate fiber detection success, we use noisy synthetic data generated with SNR 35 and with 1, 2, or 3 fibers chosen randomly with equal volume fraction and random angle between fibers set above 45°. We generate 1000 such HARDI profile separately and count the number of times we correctly detect the number of ODF maxima. For the simulations,

we also vary estimation order $\ell = 4, 6$ and 8, use b-values of 1000, 3000 and 5000 s/mm^2 and use sampling densities of $N = 81$ and 321 on the hemisphere, corresponding to a 3^{rd} and 7^{th} order tessellation of the icosahedron respectively. We also record the angular error made in degrees on each direction. Next, to evaluate angular error made on the detected maxima, we fix the fODF and fSD estimation order at $\ell = 6$ and use a simulation with $b = 3000$ s/mm^2, $N = 60$ (same gradient directions as our real data acquisition), separation angle of 60°, SNR $= 30$ and volume fraction $p_1 = p_2 = 0.5$. Finally, we show qualitative simulated results that illustrate the effect of varying HARDI signal generation parameters such as b-value, SNR, separation angle and volume fraction in Eq. 9.

3.6.3 Real Data Experiment

First, we show the effect of the deconvolution sharpening qualitatively on a regions with known fiber crossings between two and three different fiber populations. Then, we compare deterministic tracking methods DT/dODF/fODF/SPLIT-STR and probabilistic dODF/fODF-PROBA on complex fiber bundles. We study the performance of the different algorithms to reconstruct several commissural fiber tracts in one subject. Different seed masks were generated on the color coded FA maps. Fiber tracts and connectivity distributions were generated from every voxel in the mask. For the reconstruction of the fibers passing through the anterior commissure (AC), a seed voxel was placed in the mid-sagittal cross section of the AC and a second tracking was started from two seeds, one on the left and right side of the mid-sagittal cross section; for the commissural fibers connecting the contralateral inferior and middle frontal gyrus a seed voxel was defined in the mid-sagittal section of the rostral body of the CC (Talairach 0, 18, 18); for the tapetum and temporal commissural fibers we selected 4 seed voxels between the left lateral ventricle and the optic radiation close to the splenium of the CC (Talairach -22, -42, 24).

3.6.4 Quantifying the Projections of the Corpus Callosum

As an application, we investigated how the reconstruction of transcallosal fiber connections could be improved with the fODF in the group of 8 subjects. We show in which parts of the CC we can reconstruct fibers connecting the ventral and lateral parts of the cortex. These fibers cross the corona radiata and parts of the superior longitudinal fasciculus [53] and cannot be detected with the simple tensor model and are limited with the dODF. Regions of interest (ROIs) for the white matter tractography in each subject were defined by the sagittal cross section of the CC. For each seed voxel in the ROI the fODF-PROBA tractography was performed separately. To evaluate the connectivity to lateral and ventral cortical areas, The percentage of random fiber tracts reaching lateral parts of the brain (Talairach > 30) are quantified. The result is color coded on the mid-sagittal plane.

Angular resolution limitations (a)

		$b = 5000$ s/mm^2			$b = 3000$ s/mm^2			$b = 1000$ s/mm^2		
	order ℓ	fODF	fSD	dODF	fODF	fSD	dODF	fODF	fSD	dODF
$N = 81$	8	30°	33°	55°	31°	38°	58°	52°	54°	74°
	6	39°	42°	55°	42°	46°	59°	52°	58°	74°
	4	51°	52°	59°	52°	54°	63°	57°	63°	75°
$N = 321$	8	29°	32°	44°	30°	36°	50°	45°	50°	69°
	6	37°	40°	47°	38°	43°	52°	45°	55°	69°
	4	50°	50°	56°	52°	55°	60°	56°	62°	72°

Fiber detection success (b)

		$b = 5000$ s/mm^2			$b = 3000$ s/mm^2			$b = 1000$ s/mm^2		
	order ℓ	fODF	fSD	dODF	fODF	fSD	dODF	fODF	fSD	dODF
$N = 81$	8	100%	100%	78%	94%	94%	61%	86%	85%	56%
	6	99%	99%	76%	91%	90%	60%	69%	67%	54%
	4	70%	70%	62%	63%	63%	55%	62%	60%	52%
$N = 321$	8	100%	100%	96%	100%	100%	87%	95%	95%	55%
	6	100%	100%	88%	100%	100%	84%	66%	70%	53%
	4	83%	83%	62%	78%	76%	62%	58%	56%	52%

Table 1: ODF sharpening and spherical deconvolution improve fiber detection and increases angular resolution QBI. The sharp fiber ODF (fODF) and filtered spherical deconvolution (fSD) [55] have similar fiber detection and angular resolution behavior that outperform the classical diffusion ODF (dODF). We test effects of changing estimation order ℓ, b-value and spherical sampling density N. Simulations were done on 1000 HARDI profiles. In (a) HARDI profiles are generated with SNR 35 and with a random number of crossing fibers between 1, 2 and 3 and with random angle between fibers above 45°. In (b), noise-free HARDI simulations are generated with 2 fibers crossing. We report the angle between fibers under which only a single ODF maxima is detected.

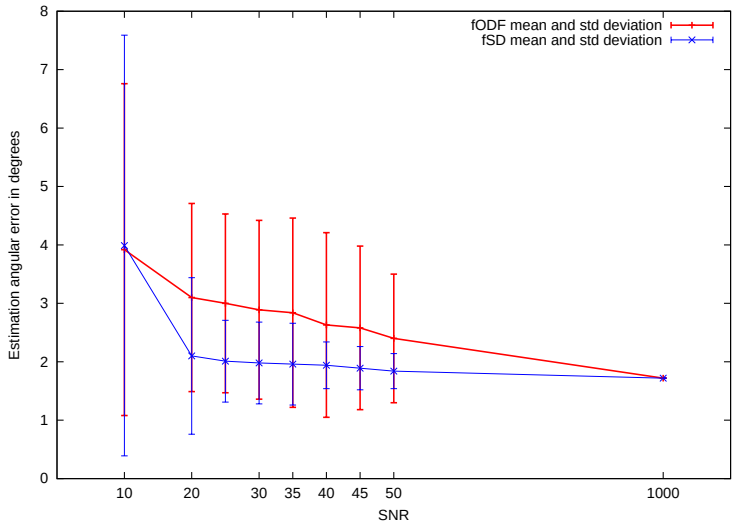

Figure 2: Effect of varying SNR on the detected maxima of the sharp fiber ODF (fODF) and filtered spherical deconvolution (fSD) [55]. We plot the mean and standard deviation of the estimated angle error for the fiber simulation with separation angle of 60°, $b = 3000$ s/mm^2 and $N = 81$.

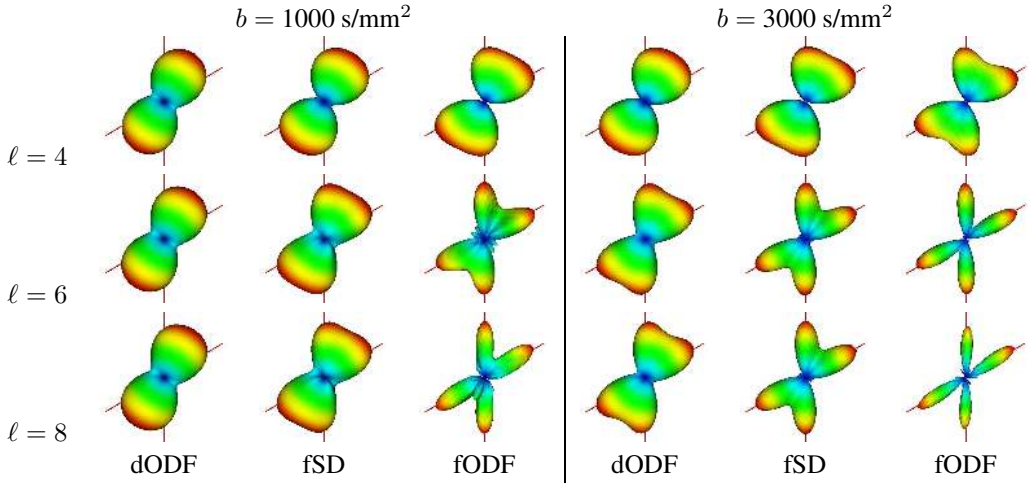

Figure 3: Effect of varying estimation order ℓ and b-value on the diffusion ODF (dODF), sharp fiber ODF (fODF) and filtered spherical deconvolution (fSD) [55].

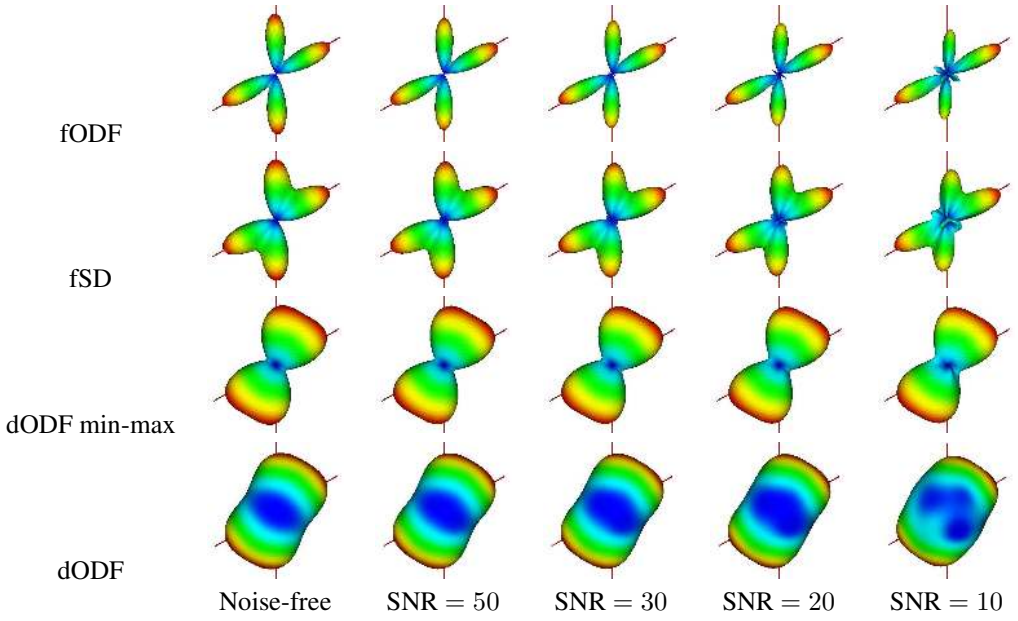

Figure 4: Effect of varying SNR on the diffusion ODF (dODF), sharp fiber ODF (fODF) and filtered spherical deconvolution (fSD) [55].

4 Results

4.1 Effect of the Deconvolution Sharpening Transformation

Synthetic Data Simulations Tbl. 1(a) first shows that the angular resolution of QBI is improved with the sharp fiber ODF by approximately 20° over all simulations. The table also shows that fODF has a slightly better angular resolution than fSD [55], with an average 5° difference in favor of the fODF. The improvement for order $\ell = 8$ is the most apparent with an increase of approximately 25° between fODF and dODF. At order $\ell = 6$, the increase is approximately 15° between fODF and dODF. As expected, the less apparent improvement is for lowest order $\ell = 4$, where the ODF is too smooth for the deconvolution sharpening to make an important difference. Moreover, it is also expected that the angular resolution increases considerably for higher b-values. However, note that the difference is very small when comparing $b = 5000$ s/mm^2 and $b = 3000$ s/mm^2 columns. Note also that increasing the sampling scheme does not make an important gain in angular resolution in this experiment. There is a difference of only a few degrees when going from sampling $N = 81$ to $N = 321$. This suggests that increasing the number of sampling directions is not important if one uses a low spherical harmonic order estimation. Finally, it is important to point out that when both the dODF and fODF successfully detect the underlying fiber populations, we record no noticeable

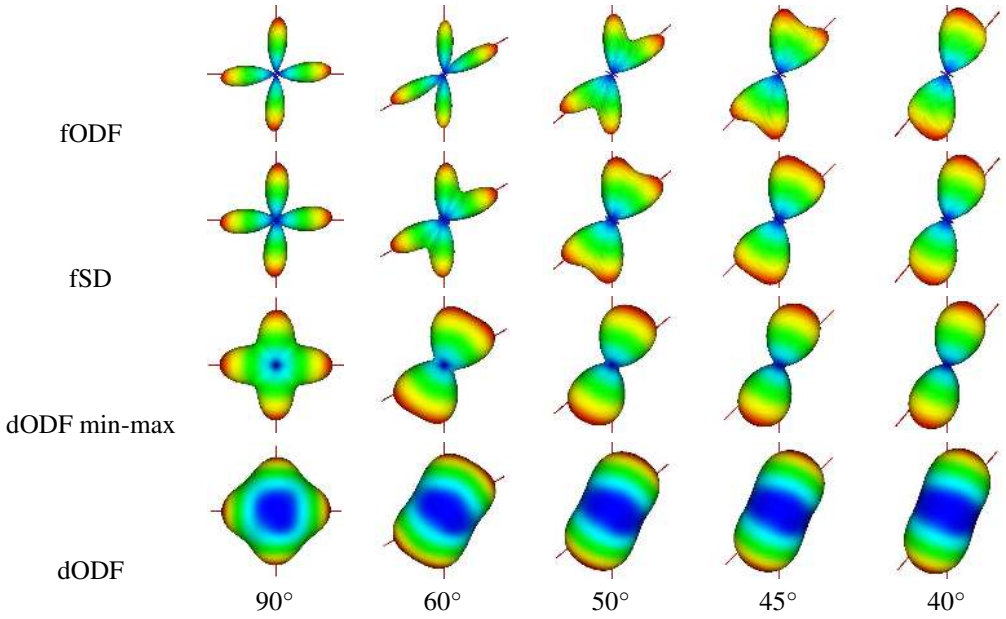

Figure 5: Effect of varying separation angle on the diffusion ODF (dODF), sharp fiber ODF (fODF) and filtered spherical deconvolution (fSD) [55].

difference in angular error made on the ODF maxima, i.e. the sharpening does not introduce errors on the detected maxima.

Then, Tbl. 1(b) shows that sharpening increases the success rate of fiber detection in the synthetic data simulation described in Section 3.6.2. We also see that the fODF and fSD have very similar success rate in this simulation. The fODF has better success rate than fSD some cases because it has a slightly better angular resolution limitation. The more important increase in success rate occurs for high estimation order. In particular, for b-value 1000 s/mm^2, order $\ell = 8$ and sampling $N = 321$ there is an increase of 40% and for $b = 3000$ s/mm^2, $\ell = 6, 8$ and $N = 81$ there is an increase of more than 30% between fODF and dODF. Note that sharpening the b-value 1000 s/mm^2 data has the effect of improving fiber detection to above the level of b-value 3000 s/mm^2 data without sharpening for most order estimations and similarly, when comparing the dODF column at $b = 5000$ s/mm^2 and fODF column at $b = 3000$ s/mm^2. Moreover, increasing the spherical sampling density N increases the success rate of fiber detection. This is more apparent at high order $\ell = 8$ and for b-value > 1000 s/mm^2 for the dODF. Finally, note also that, for a given b-value, the fODF column at a low sampling $N = 81$ has better fiber detection success than for the dODF column at high sampling $N = 321$.

Next, Fig. 2 shows the effect of noise on the angular error of detected maxima from fODF and fSD. We do not plot the curve for the dODF as it overlaps the fODF curve. The fSD and fODF curve

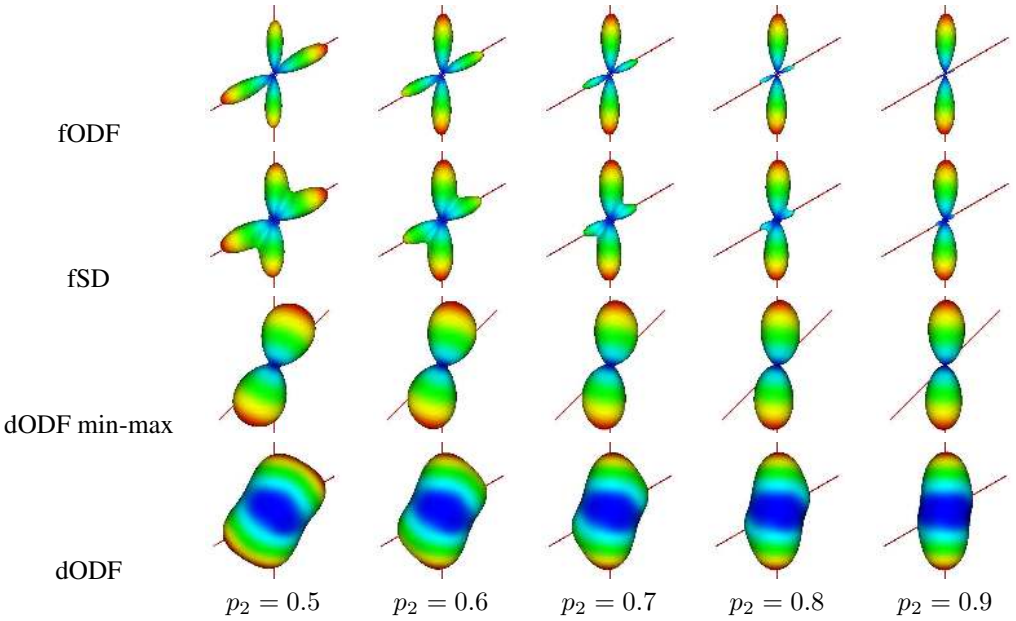

Figure 6: Effect of varying volume fraction on the diffusion ODF (dODF), sharp fiber ODF (fODF) and filtered spherical deconvolution (fSD) [55].

have a similar profile but we see a small improvement of approximately 1 to 2° in angular error. Note that the ODF maxima are detected using a fine mesh with 1281 sampling on the hemisphere, giving roughly 4° between each mesh point. Overall, the mean angular error is thus less than an angular sample.

Finally, figures 3-6 qualitatively show the effect of varying the HARDI signal parameters on the dODF, fODF and fSD reconstructions. In these synthetic simulations, the tensor profiles were estimated from our real data. From the 300 voxels with highest FA value, we found an average FA of 0.7 and an average eigenvalue ratio of $e_2/e_1 = 0.26$. We use simulations with $N = 60$, $b = 3000$ s/mm^2, separation angle of $60°$, equal volume fraction $p_1 = p_2 = 0.5$ and then vary independently the b-value, SNR, separation angle and volume fraction. Note that figures 3-6 confirm quantitative observations made from Tbl. 1. The angular resolution gain of the fODF over dODF is striking. Also, the fODF profile is overall more sharp than the fSD profile. However, it is possible to see that fODF peak is not always as well aligned with the true direction as it is for the fSD. In particular, Fig 3 shows the difference in the reconstruction when changing estimation order ℓ and b-value. As expected, the best angular resolution is obtained for high ℓ and high b-value. However, for $\ell = 8$, spurious peaks due to noise become more important. We thus choose to fix the order at $\ell = 6$ and $b = 3000$ s/mm^2 for the other simulations. Fig. 4 shows that the fODF reconstruction is robust to noise. Even at low SNR, the angular resolution is conserved and the spurious peaks effect is

not dramatic for SNR > 10. We fix SNR 30 for other simulations. Fig 5 qualitatively shows the gain in angular resolution between fSD and fODF. The fODF is able to better discriminate the two fiber compartments at separation angle of 45° and fSD seems limited below separation angle of 50°. Finally, Fig 6 shows that fODF is able to discriminate fiber compartments clearly for equal fractions up to volume fraction of 30%. For smaller fractions only a single compartment is detected. All these simulations and figures agree with published results in [14, 55, 56].

Therefore, the sharpening deconvolution improves QBI considerably. Our synthetic data simulations show that crossing fibers are more easily detected and that the angular resolution limitation is improved with the fODF. The sharpening transformation has the desired effect of enhancing the underlying fiber population, which makes it easier to detect crossing fiber configurations with smaller separation angle. Compared to fSD [55], the fODF behaves similarly while working direct on the dODF and not on the signal. The fODF has a slightly better angular resolution and fSD makes slightly less angular error on the detected maxima.

Real Data Experiment Fig. 7a qualitatively shows the effect of the deconvolution sharpening transformation on a single voxel of our real dataset. This voxel was selected at the interface between the fibers to the lateral motor stripe and the SLF (Talairach -34 -4 29). We see that the dODF find only one maxima but that there seems to be another single fiber compartment with less volume fraction. The fODF is able to discriminate the second fiber compartment and the recorded separation angle is 62°. As the estimation order increases, the second fiber compartment is more evident at the cost of spurious peaks appearing for $\ell = 8$. We again see that fiber detection and angular resolution are improved with the deconvolution sharpening transformation.

Fig. 7b shows the multidirectional information coming from the diffusion ODF and the sharp fiber ODF on a region of interest in a coronal slice (Talairach -4) of the human brain dataset. In this ROI, the CC forms the roof of the lateral ventricles and fans out in a massive collateral radiation, the corticospinal tract (CST) lies lateral to the ventricle and is directed vertically and the SLF crosses the base of the precentral gyrus in anterior-posterior direction. The lateral projections of the CC cross the CST and the SLF. Fibers of the SLF partly intersect with the fibers of the CST and the CC. Some voxels of the dODF and fODF in area (a,a') contain these three fiber bundles crossing. It is thus surprising that recent work [8] report no voxels with three crossings. In fact, area (a) in this ROI, contains a large strip of voxels with low FA < 0.15 running at the medial border of the SLF, where crossings with three fiber populations are detected in the fODF. Overall, the fODF recovers more voxels with 2-fiber crossings than the dODF. In fact, in a mask of the white-matter, we detect twice as many voxels with two fiber populations with the fODF estimation when compared with the dODF reconstruction.

4.2 Tracking

In this section, we compare and study tracking results from the deterministic tracking algorithms, DT-STR, dODF-STR, fODF-STR, and SPLIT-STR of Section 3.3, and from the probabilistic tracking algorithm, dODF-PROBA and fODF-PROBA of Section 3.4. The tracking is performed on a synthetic branching data example and on human white matter fiber bundles with known crossings in

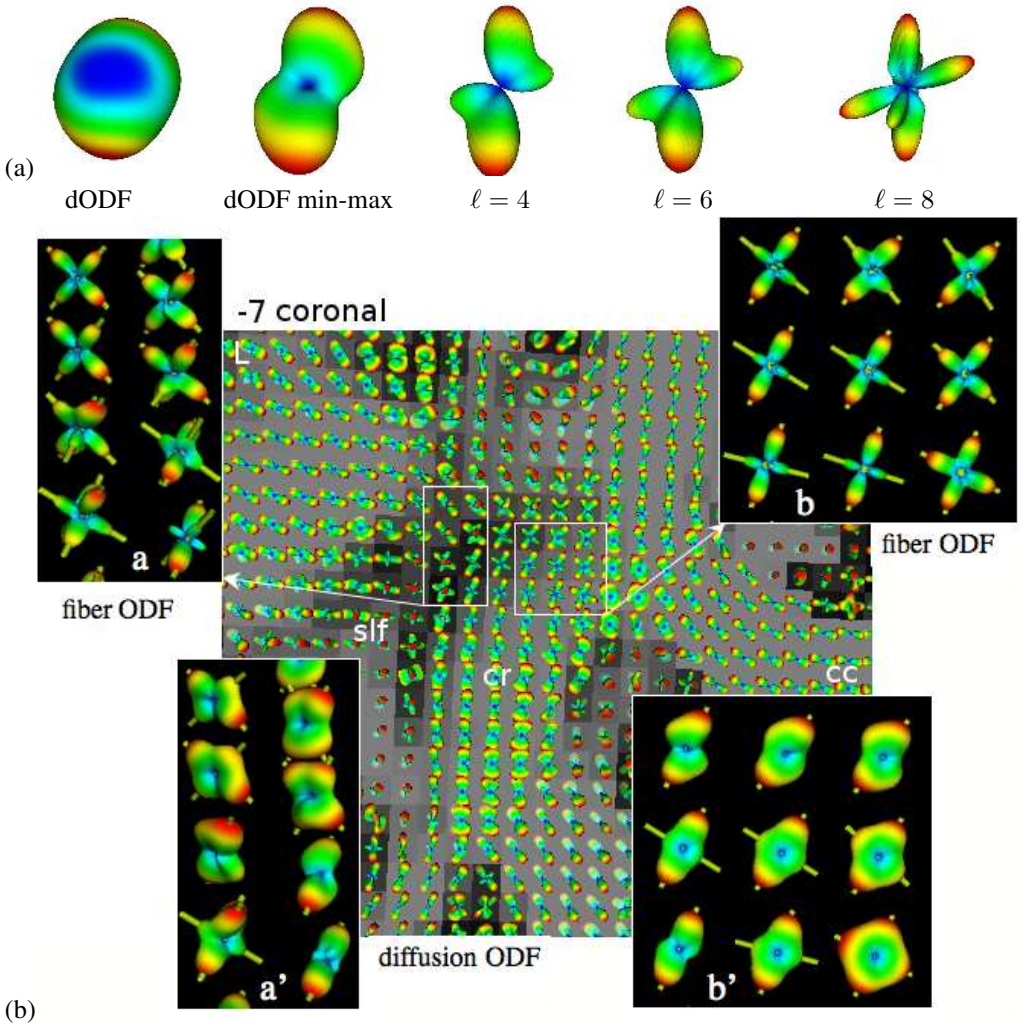

Figure 7: Deconvolution sharpening on real data improves fiber detection of QBI by increasing angular resolution. In the (1), the second maxima is missed in the diffusion ODF (dODF) and min-max normalized dODF. With sharpening, the second fiber direction is identified even at low orders of $\ell = 4$ and $\ell = 6$. The real data voxel in (a) was manually selected by an expert at the interface between motor stripe and superior longitudinal fasciculus. In (b), there are more crossings detected using the fiber ODF (a,b) than dODF (a',b'). The ROI shows crossings between the cortical spinal tract / corona radiata (cst/cr) (going up in the plane), superior longitudinal fibers (slf) (coming out of the plane) and the lateral projections of the corpus callosum (cc) (in the plane). (a,a') are tilted to see the fiber directions more clearly.

regions where DT-based algorithms are limited. Overall, we observe three results: 1) fODF-PROBA and SPLIT-STR are able to track through fiber crossings and recover crossing, fanning and branching fiber configurations, 2) SPLIT-STR and fODF-PROBA are better than dODF-based and DT-based tracking in regions of fiber crossings, and 3) fODF-PROBA has the classical advantages of probabilistic algorithms over deterministic SPLIT-STR and also is able to recover many projections from the CC to lateral areas of the cerebral cortex.

4.2.1 Deterministic ODF-based Tracking

Fig. 8a shows the limitations and differences of DT-STR results compared to the fODF-STR and SPLIT-STR results. Tracking was started at the bottom of the branch in all cases. Note that where DTs are prolate with principal direction not agreeing with the true fiber orientations, the ODFs have multiple maxima that match with the underlying fiber population. Hence, the path followed by DT-STR is wrong and follows a false direction that takes it to the middle of the branch. Had there been another structure behind the branching fibers, the tract could have easily leaked in the other structure and diverged. On the other hand, fODF-STR has the advantage of following the right direction. If there are two possible orientations, it goes in direction closest to its incoming direction. On the other hand, SPLIT-STR splits and follows both ODF directions when possible which recovers the full branching structure. It is interesting to note the difference between dODF and fODF streamlines in the crossing area. The fODF-STR splitting occurs several voxels lower in the branching where the separation angle between the two fiber compartments is lower than 60°. Finally, we see that the tractogram of the fODF-PROBA for three different initialization. The fODF-PROBA is not very sensitive to initialization and able to recover the branching structure starting from voxels at the left, middle and right of the structure. Note that there is a flaying of tracts from one parallel fiber to the neighboring fibers within the synthetic bundle. This is expected from probabilistic tracking and this is why one typically thresholds the tractogram to obtain the most probable tracts.

Fig. 8b shows a branching fiber configuration in the same ROI as seen in Fig. 7. One set of tracts (red fibers) are started from a voxel in the CC and another set of tracts are started from a voxel in the CST (green/yellow fibers). As expected, SPLIT-STR recovers the branching configuration of both fiber tracts and recovers fibers projecting in motor areas in two gyri. On the other hand, fODF-STR is able to step through the crossings whereas dODF-STR and DT-STR are limited. Both fibers starting from the CST and from the CC take the average direction of the two ODF orientations and projects only the medial motor cortex. tracking. The angle between fiber compartments is between 60 and 80° in that area and the dODF cannot discriminate clearly the two fiber populations.

4.2.2 Probabilistic Tracking

Anterior Commissural Fibers Tracking of the anterior commissural (AC) fibers in Fig. 9 shows the advantages of the fODF-PROBA tracking over dODF-PROBA and DT-STR tracking. dODF-PROBA and DT-STR are blocked close to the seed point by low FA areas. Particles of dODF-PROBA cannot propagate to the temporal poles because the paths are diffusive and leak outside the anterior commissural bundle, which is only a few voxel wide around the seed point. However, with a multiple seeding approach, DT-STR and dODF-STR are able to recover both paths to the

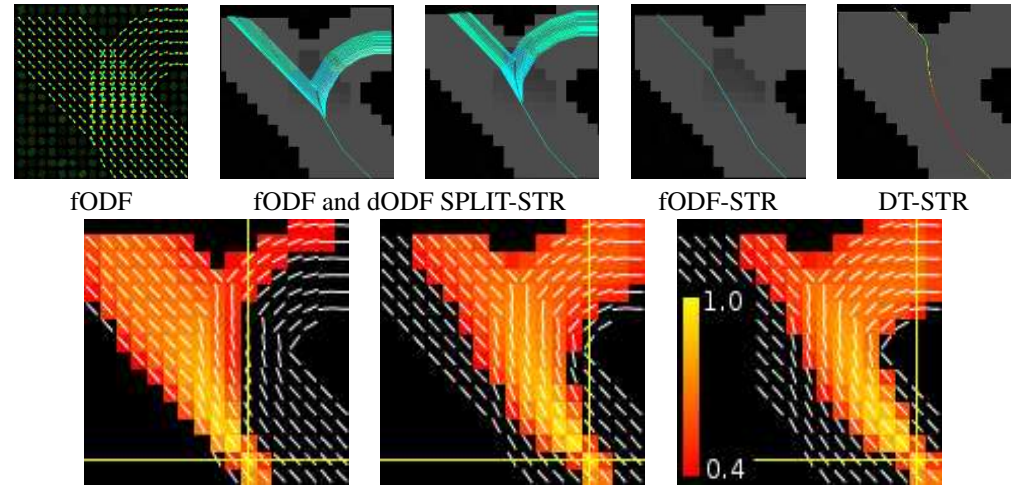

Figure 8: SPLIT-STR is able to recover the known fiber fanning configurations. In (a), deterministic tracking was started at the bottom of the branch in all cases. HARDI data was generated with b-value of 3000 s/mm^2, $N = 81$ and SNR 35. fODF-PROBA was also done with 3 different initializations overlaid on DT principal eigenvector. fODF-PROBA is not particularly sensitive to initialization. In (b), SPLIT-STR recovers known branching configurations to the two motor gyri from both seed points. We have colored fibers starting from the CC in red and fibers starting from the CST in green/yellow.

temporal poles, as published in Catani et al [12]. In contrary, deterministic fODF-STR and SPLIT-STR tracking can reconstruct the fibers connecting the temporal pole via the AC from a single seed point in the mid-sagittal cross section. Probabilistic tractography done with the fODF suggest

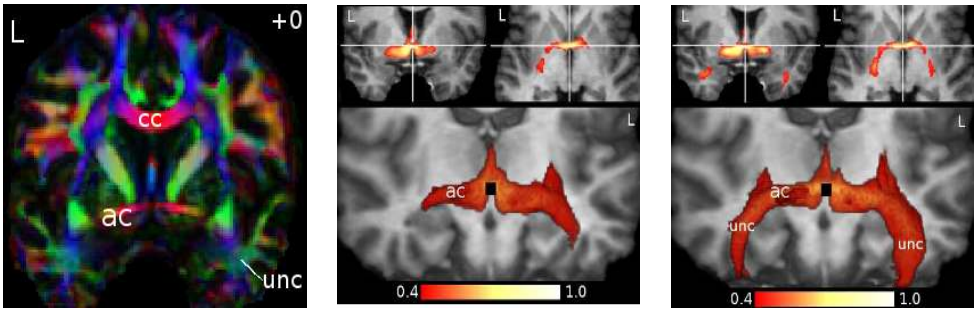

FA-RGB map | dODF Tractogram | fODF Tractogram

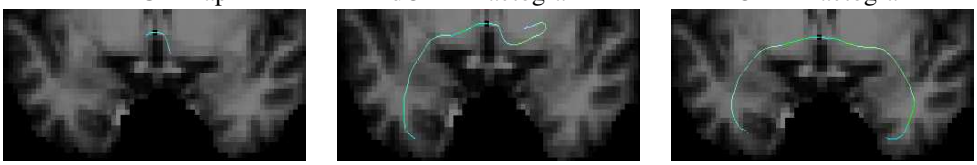

DT-STR | dODF-STR | fODF-STR

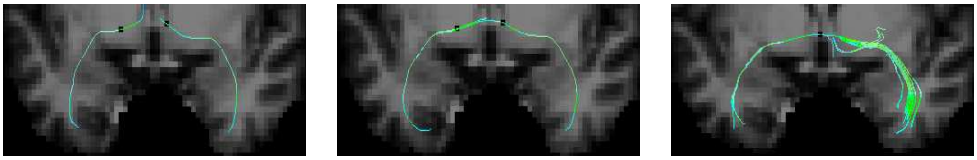

2 seed DT-STR | 2 seed dODF-STR | SPLIT-STR

Figure 9: Tracking of the anterior commissure fibers (ac). Probabilistic tracking is shown on coronal and axial slices through the ac. We also show a 3D rendering of the tractogram iso-surface. fODF-Proba reaches the temporal pole close to the uncinate fasciculus (unc) whereas dODF-Proba can only reconstruct a small part. Deterministic tractography needs multiple seeding initialization in the DT and dODF case due to the small diameter of the ac on this subject.

additional projections to more posterior parts of the temporal lobe and through the anterior subinsular white matter to the inferior occipitofrontal and inferior longitudinal fascicle. Moreover, a second anterior pathway was found on the right hemisphere for this subject (Fig. 9, top row middle and right).

Callosal fibers to the inferior and middle frontal gyrus DT-STR and fODF-STR tracking can only find the commissural fibers connecting the medial parts of the frontal lobe (Fig. 10, second row, left and middle). Fanning of the fiber bundle to the inferior and middle frontal gyrus was found with the SPLIT-STR method on the left hemisphere and to a lower extent on the right. The tractogram computed with the fODF-PROBA method reveals a strong interhemispheric connection of the lateral parts of the frontal lobe. Additional fibers are found branching to the anterior thalamic

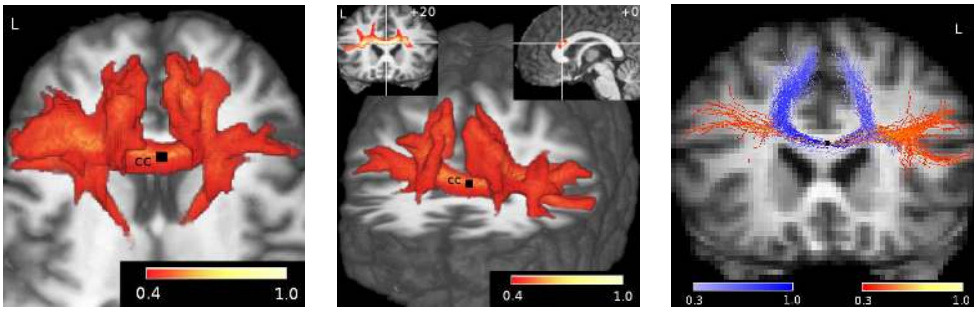

Tractogram top view | top-left-front view | fODF-PROBA fibers

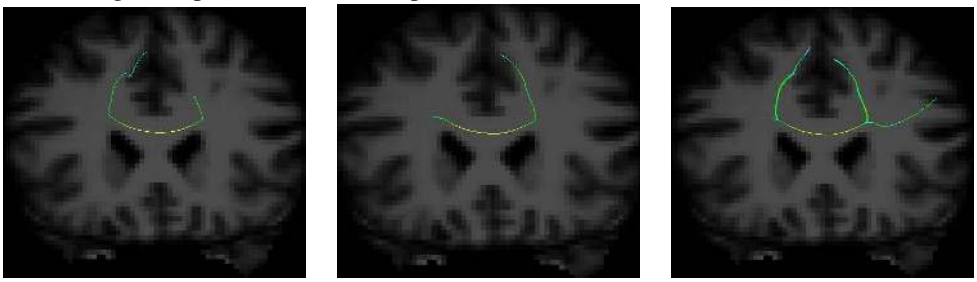

DT-STR | fODF-STR | SPLIT-STR

Figure 10: Tracking of the projections of the corpus callosum to Broca's area. The probabilistic tractogram is shown on a coronal and sagittal slice and as 3D rendering. The tractogram shows asymmetry with stronger connections to the left inferior and middle frontal gyrus than to the homolog area. We also show a selection of the probabilistic fibers colored differently depending on their end point projections to the lateral or medial areas. From the deterministic methods only SPLIT-STR can reconstruct this complex structure.

radiation (Fig. 10, top left). Fig. 10, top right shows sample fiber tracts included in the probability map (left, middle).

Callosal fibers to the temporal lobe Fig. 11 shows the fibers in the splenium of the CC, which sweep inferiorly along the lateral margin of the posterior horn of the lateral ventricle which form the tapetum. These fibers are in close contact to the commissural fibers connecting the precuneus of both hemispheres. On the left hemisphere the splitting is close to the 4 voxel seed region and all methods can bind both parts. Only SPLIT-STR and fODF-PROBA can reconstruct the splitting in both hemispheres to the bundles connecting the temporal lobe and the parietal lobe. The fibers to the temporal lobe split to the transverse temporal (Heschel's) gyrus and to the inferior longitudinal fasciculus. Probabilistic tractography also suggest a close relation to the posterior thalamic radiation.

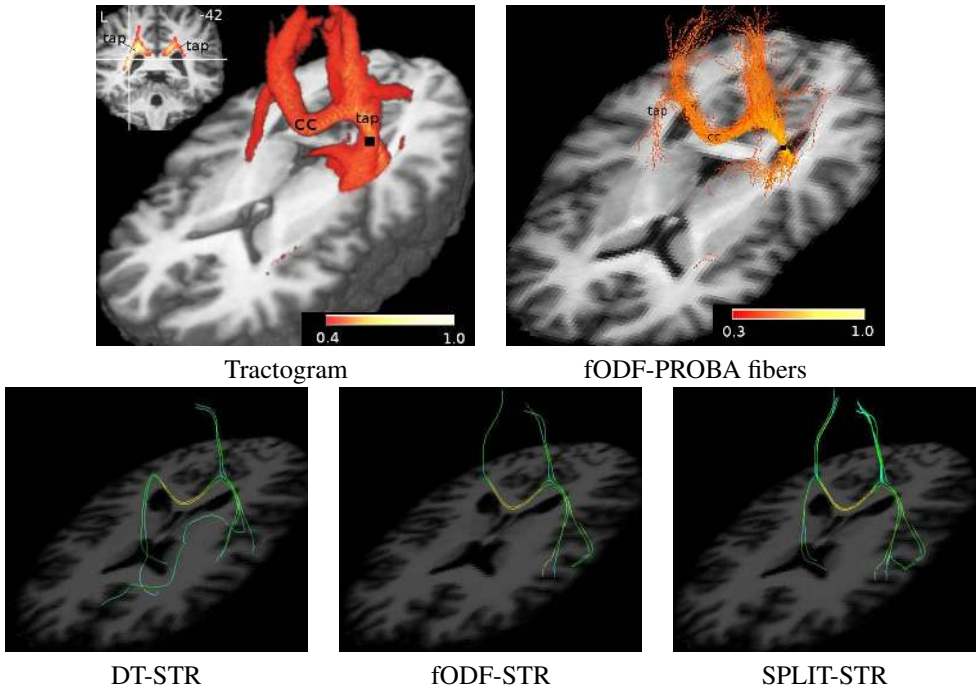

Figure 11: Probabilistic tractogram of a single seed point in the tapetum (tap) reconstructs the fibers crossing the cc and connecting both temporal lobes. Deterministic tracking was initialized from 4 seed points in the tapetum. SPLIT-STR reconstructed this complex structure.

4.3 Quantifying Lateral Projections of the Corpus Callosum

Fig. 12 shows the color labeling of the ROI indicating regions with strong lateral connectivity. The color corresponds to the percentage of fibers which cross a para-sagittal plan (Talairach > 30) as indicated by the lines on the coronal slice. For all subjects a maximum number of lateral fibers was found in the genu or the rostral body of the CC connecting the inferior and middle frontal cortex and the premotor cortex. The callosal fibers interdigitates with the fibers of the corona radiata. The tractogram for the voxel with the most lateral connections shows fibers to the left and right middle frontal gyrus and the left inferior frontal gyrus in addition to the connections of the medial frontal cortex. The proportion of lateral fibers in this voxel is $20\% \pm 6\%$ for the 8 subjects.

A second peak (bright color) was found in the isthmus or splenium of th CC connecting the temporal areas. The corresponding fibers lie deep to the optic radiation in the tapetum and connect the temporal lobe and in particular to the auditory cortex. The proportion of temporal fibers in this voxel is $30\% \pm 10\%$ for the 8 subjects.

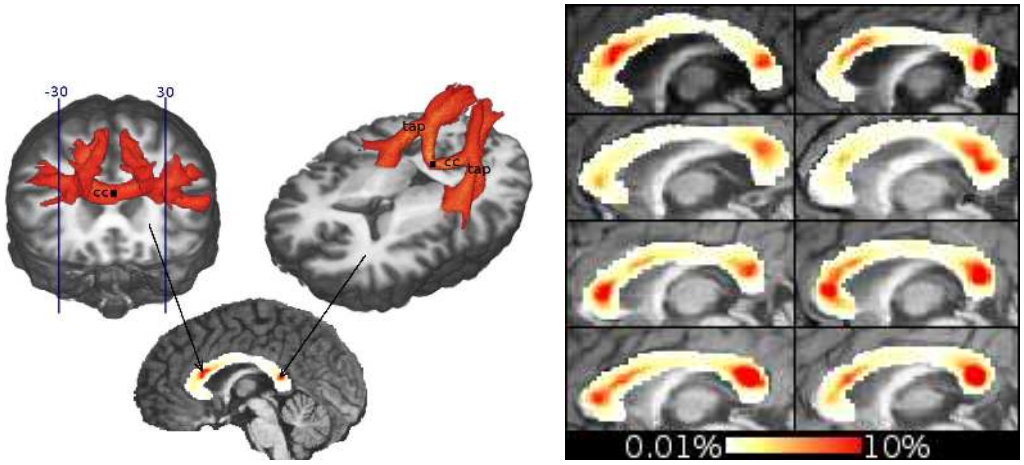

Figure 12: Quantification of the ratio of lateral fibers (Talairach > 30) in the different parts of the corpus callosum (cc) typically completely missed in DT tractography. All 8 subjects show strong lateral connectivity in the genu or the rostral body of the cc and a second peak in the splenium. fODF-PROBA finds more than 10% of lateral fibers in large parts of the cc.

5 Discussion

We have proposed an integral concept for tractography of crossing and splitting fiber bundles in the brain based on the sharp fiber ODF reconstruction from QBI. First, we have developed a new deconvolution *sharpening* transformation from diffusion ODF (dODF) to *sharp fiber* ODF (fODF) from regularized and analytical estimation of the ODF [18]. Then, we have showed that the fODF considerably improves fiber detection and angular resolution compared to the standard dODF by approximately 20°. We have also showed that the fODF behaves very closely to the filtered spherical deconvolution (fSD) estimation of the FOD. We have compared the dODF, fODF and fSD reconstructions methods and reproduced simulated results published in the literature. Finally, we have extensively compared both new tracking algorithms and have performed expert visual validation on complex fiber bundles of a human brain dataset. In particular, we illustrated an important application for the modeling of interhemispheric cognitive networks with a quantification of the projections of the corpus callosum. We have quantified regions of the corpus callosum where we are able to recover fibers projecting to the lateral cortex.

We have proposed an important improvement of QBI. The standard Q-ball dODF reconstruction is smooth with large contributions outside the principal directions of diffusion. Even after min-max normalization, the dODF has poor angular resolution, especially at lower b-values. Hence, this dODF is not necessarily the best object to be working with if one is interested in the underlying fiber population. To our knowledge, our sharpening deconvolution is the first attempt to transform

the diffusion ODF into a fiber ODF. We now have the distribution of the relative importance of each fiber in a voxel instead of having an orientation distribution of the diffusion in each direction.

The deconvolution sharpening is well-defined and the dODF kernel is estimated directly from the real data. Therefore, we have very few parameters to set in this approach. One only needs to choose the approximation order ℓ of the signal and the regularization parameter [17, 18]. This makes the fODF estimation fast and robust when working with spherical harmonics. The powerful tool was again the Funk-Hecke theorem, as in the derivation of our previous analytical ODF solution [18]. This theorem allows to solve the integral on the sphere between the single fiber diffusion ODF kernel and any spherical harmonic.[1] The final fODF is a simple linear transformation of the coefficients of the dODF.

Therefore, anybody working with QBI and/or a diffusion ODF can benefit from our work and apply our sharpening transformation to obtain a fiber ODF. It is important to point out that spherical deconvolution (SD) is another method to obtain a fODF, also called FOD (fiber orientation density) in the SD literature [1, 3, 14, 34, 50, 55, 56]. In this work, we have compared our sharp fODF to the filtered spherical deconvolution (fSD) of Tournier et al [55]. Our simulations compared the effect of varying b-value, estimation order, SNR, separation angle and volume fraction. We have showed that our fODF produces stable profiles that are very similar to those obtained from fSD. Quantitatively, we found that the fODF has slightly better angular resolution of approximately 5° while making a slightly larger angular error on the detected fiber direction of approximately 1.5°.

In our sharp fODF reconstruction, we have two mechanisms that limit the spurious peaks and negative values effect problems observed in the deconvolution methods[2]. First, we choose to focus on low order estimations of the ODF, i.e. we use a 4th or 6th order estimation of the fODF. We find that the trade-off between noise in the higher order frequencies and gain in angular resolution is not necessary for our tractography application, especially in the case of probabilistic tracking. Moreover, the best results in our real data experiments are obtained for estimation order $\ell = 4$. It also has the advantage of a very fast fODF estimation (less than 20 seconds on the real dataset) and good compression properties because we only need to store 15 coefficients at every voxel. Note that Tournier et al [55, 56] mostly consider high estimation orders of $\ell = 8$, 10, 12. Thus they need to filter high order frequencies [55] or very recently use a positivity constraint with super-resolution on the spherical deconvolution [56] that also improves the angular resolution. A second mechanism that limits the effect of spurious peaks in our solution is the Laplace-Beltrami regularization included in the estimation of the spherical harmonic coefficients describing the HARDI signal [17, 18]. This regularization is in a similar spirit as the gradient constraint regularization recently proposed in [50]. Note that we have fixed our regularization parameter to keep a fast solution but we could have also used L-curves [17] or other methods to estimate the optimal regularization parameter at every voxel, as in [50]. Overall, we have showed that our fODF is robust to spurious peaks and negative values on the sphere by using a low approximation order and a regularization parameter. It is part of current work to see how we can theoretically eliminate negative values and spurious peaks appearing at higher harmonic orders and see if it is possible to do so while working directly on the harmonic

[1] Note that with a very similar derivation, one can also use the Funk-Hecke theorem to solve the spherical deconvolution to reconstruct the FOD of Tournier et al. [55] without the need for rotational harmonics.

[2] Dell'Acqua et al [14] use a Richardson-Lucy numerical method that forbids negative values on the sphere.

coefficients without having to project on the sphere and without the need for iterative algorithms [15, 56].

In this paper, we showed that it is possible to resolve and improve fiber crossing detection on a real dataset with a low sampling scheme and a low b-value (60 DW images and $b = 1000$ s/mm^2). In theory, Q-space imaging methods need the narrow pulse approximation and in particular, QBI approximation of the diffusion ODF is best for high b-values. Although not shown here, we are also able to resolve fiber crossings from datasets with 81 DW images and b-value of 1000 s/mm^2 (data presented in [17]) as well as clinical datasets with 41 DW images and b-value of 700 s/mm^2 from a 1.5 T scanner[3]. Therefore, the fact that the sharp fiber ODF estimation is fast and simple to implement and that it can resolve fiber crossings in datasets with low b-values and low spherical sampling schemes is promising for potential clinical applications of QBI.

Our proposed fODF is thus a good function to be used for tractography. We have used it in both our deterministic and probabilistic tracking extensions of previous DT-based methods. We clearly showed that the results are improved over standard DT-based methods. In the deterministic case, the fODF has a better angular resolution and the maxima of crossing and splitting fiber bundles are detected more easily. Hence, we showed that SPLIT-STR can follow more multiple maxima and recover most of fanning structures in the regions studied. Although sensitive to initialization, SPLIT-STR tracking was able to recover similar bundles as the fODF-PROBA method in most cases.

SPLIT-STR is thus an efficient and easy way to obtain a good idea of fiber tracts starting from only a few seeds. The underlying assumption of SPLIT-STR is that all multiple peaked fiber ODF have an underlying branching structure, which makes it reasonable to follow all available maxima at each step. This is the reason for using a curvature threshold of the tracts of 75° instead of 90°. This threshold avoids following tracts through "pure" crossing configurations where we know that we are then stepping into unwanted fiber bundles. This raises questions for multidirectional deterministic tractography: Should the tracking algorithm split as much as possible to recover as much fiber structure as possible before clustering and post-processing the tracts to separate them into bundles? Or, should the tracking have a built-in scheme to differentiate the different sub-voxel crossing possibilities and decide whether or not a tract should be split in the tracking process? For instance, split in the case of a branching bundle but not split in the case of a crossing fiber because it is assumed that it steps into a different fiber bundle. Information about the local geometry, curvature and torsion of tracts can help for this problem [51] and in [52], preliminary results are obtained discriminating crossing and branching sub-voxel fiber configurations.

To deal with the uncertainty in the dODF or fODF maxima, a probabilistic approach is more robust. In a probabilistic case, the sharpening operation has its greatest importance just as it is in probabilistic DTI tracking [4, 35, 38, 54]. For DTI probabilistic tracking, heuristic sharpening taking a power of the diffusion tensor is done to obtain a tensor representing the fiber distribution, which is crucial to obtain decent tracking results.[4] Similarly, in ODF-based probabilistic tracking, the tractograms are diffusive and leak into unwanted bundles if done without sharpening. However, this leaking effect is not as dominant in probabilistic ODF tracking as it is probabilistic DTI tracking.

[3] Datasets of the public QBI database of Poupon et al [47]

[4] Note that this DTI sharpening can also be done with spherical deconvolution applied on the spherical harmonic representation of the diffusion tensor [20].

The min-max normalization of the sampled dODF values to the range between 0 and 1 removes the isotropic part and the shape of the dODF is sharpened. However, this min-max normalization subtracts a different value from each ODF and might introduce artifacts to the probabilistic tracking result. The shape and width of the lobes of the min-max dODF do not correspond to the fiber distribution in the voxel. We believe that the spherical deconvolution of the dODF by the diffusion kernel estimated directly from the diffusion signal of single fiber population is the natural transformation of the dODF to a sharp fODF. This sharpening also removes the isotropic part of the ODF and improves the angular resolution of crossing fiber distributions.

Microscopy of white matter shows that the nerve fibers are not completely parallel within a bundle. Probabilistic tractography includes this incertitude. The reconstructed fibers spread out to neighboring voxels within the hole cross section of a fiber bundle. This makes the algorithm robust to the initialization. Different starting points within an area to the same bundle lead to similar tracking results. The spreading of the tractography to the hole bundle enables the segmentation of the selected fiber bundle in its total extent. This is a clear advantage over deterministic tracking. In deterministic tracking, the sensitivity to initialization has to be solved with multiple initialization using a larger starting region and a combination of target regions.

The probabilistic tractogram is an intuitive representation of the result when overlaid on anatomical slices. This visualization allows to look at the exact location of the fiber bundle. Moreover, a 3D rendering of the iso-surface of the probabilistic tractogram gives an overview of the location and the branching structure of the fiber bundles starting from the initial seed point. The connectivity index from the tractogram also allows a quantitative comparison of the connectivity profiles from different seed points. This is at the heart of the connectivity-based cortex parcellation of [4]. The quantitative connectivity measure between a seed and a target voxel or region provided by the tractogram can be combined with functional connectivity to study cortical networks. In counterpart, probabilistic tractography suffers from connectivity values decreasing with the distance from the initial seed point due to the fanning of fiber bundles. It is part of current work to study this open problem.

For all these reasons, although slower than SPLIT-STR, we find that fODF-PROBA is more convenient to use for tractography. Overall, the tracking is less sensitive to initialization and the tractogram output more informative than the 3D curves output by SPLIT-STR. fODF-PROBA is thus a very good tool to study specific fiber bundles and compare the projections for many subjects. In particular, for fiber tracts which are known to intersect with other bundles like the callosal fibers, DT-based tractography can only reconstruct a part of the fibers or might even find wrong connections in the intersection position. We were able to show areas of the CC where classical DT-based propagations as well as SPLIT-STR and fODF-STR were limited by the intersection with the corona radiata and the superior longitudinal fasciculus. We show that we can find fibers from the lateral cortex in a major part of the CC. Current DT-based methods neglect these fibers completely (at least in the frontal lobe), which might lead to wrong interpretations of the brain functions. This important contribution opens to many neuroscience perspectives and applications. It is now important to continue this type of experiment and focus on complex fiber bundles involved in specific functional tasks where DTI tracking is in most cases very limited.

Acknowledgments Thanks to the Max Planck Institute for Human Cognitive and Brain Sciences, Leipzig, Germany and in particular to Timm Wetzel for providing the diffusion-weighted MR datasets. Part of this work was supported by PAI Procope. Finally, this work was partly supported by the diffusion MRI ARC.

A Funk-Hecke Theorem

Let $f(t)$ be continuous on $[-1,1]$ and Y_ℓ any spherical harmonic of order ℓ in $\mathcal{C}^3$, the space of 3D complex functions. Then, given a unit vector $\mathbf{u}$

$$\int_{|\mathbf{w}|=1} f(\mathbf{u}^{\mathrm{T}}\mathbf{w})Y_\ell(\mathbf{w})d\mathbf{w} = \lambda(\ell)Y_\ell(\mathbf{u}), \qquad \text{where} \qquad \lambda(\ell) = 2\pi \int_{-1}^{1} P_\ell(t)f(t)dt \tag{10}$$

and P_ℓ the Legendre polynomial of degree ℓ.

B Diffusion ODF Kernel for Sharpening

Assuming that a Gaussian can describe the diffusion of water molecules for a single fiber, as in DTI, the corresponding diffusion signal that would be measured in direction $\mathbf{u}$ is $S(\mathbf{u}) = e^{-b\mathbf{u}^{\mathrm{T}}\mathbf{D}\mathbf{u}}$. Without loss of generality, we assume that the fiber is aligned with the z-axis and it has a profile with eigenvalues $[e_2, e_2, e_1]$ ($e_1 >> e_2$),

$$\mathbf{D} = \begin{pmatrix} e_2 & & \\ & e_2 & \\ & & e_1 \end{pmatrix},$$

This profile is estimated directly from the real data, taking 300 voxels with highest FA value as we are confident that there is a single fiber population at those locations. In that case, it is easy to show that the corresponding diffusion ODF, Ψ, is given by

$$\Psi(\mathbf{u}) = \frac{1}{Z}\sqrt{\frac{1}{\mathbf{u}^{\mathrm{T}}\mathbf{D}^{-1}\mathbf{u}}}, \tag{11}$$

where Z is a normalization constant [16, 18, 58]. Now, we have

$$\mathbf{u}^{\mathrm{T}}\mathbf{D}^{-1}\mathbf{u} = \frac{1}{e_2}\sin^2\theta + \frac{1}{e_1}\cos^2\theta, \tag{12}$$

where $\mathbf{u} = [x, y, z]^{\mathrm{T}}$ with $x = \cos\phi\sin\theta, y = \sin\phi\sin\theta, z = \cos\theta$.

$$\Psi(\theta) \quad = \quad \frac{1}{Z}\left(\frac{1}{e_2}\sin^2\theta + \frac{1}{e_1}\cos^2\theta\right)^{-\frac{1}{2}} = \frac{1}{Z}\left(\cos^2\theta(e_2 - e_1) + e_1\right)^{-\frac{1}{2}}. \tag{13}$$

Letting $t := \cos\theta$ represent the dot product between the direction of the fiber and the point of evaluation, $\Psi(t)$ is defined for $t \in \{-1, 1\}$. This is the domain we need to apply the Funk-Hecke formula to. We thus define the diffusion ODF kernel as

$$R(t) := \Psi(t) = \frac{1}{Z}\left((e_2/e_1 - 1)t^2 + 1\right)^{-\frac{1}{2}}, \quad \text{where} \quad Z = \int_{-1}^{1}\left((e_2/e_1 - 1)t^2 + 1\right)^{-\frac{1}{2}} dt. \tag{14}$$

Therefore, the Funk-Hecke integral between diffusion ODF kernel and spherical harmonic of Eqs. 5 and 10 is

$$\lambda(\ell_j) = 2\pi \int_{-1}^{1} P_{\ell_j}(t)R(t)dt \quad = \quad \frac{2\pi}{Z}\int_{-1}^{1} P_{\ell_j}(t)\left((e_2/e_1 - 1)t^2 + 1\right)^{-\frac{1}{2}} dt, \tag{15}$$

which can be solved analytically using MAPLE. Due to the normalization factor Z, the diffusion ODF kernel only depends on the ratio between the eigenvalues, e_2/e_1.

References

[1] D. C. Alexander. Maximum entropy spherical deconvolution for diffusion mri. In *Image Processing in Medical Imaging*, pages 76–87, 2005.

[2] D.C. Alexander. Multiple-fibre reconstruction algorithms for diffusion mri. *Annals of the New York Academy of Sciences*, 1046:113–133, 2005.

[3] A.W. Anderson. Measurements of fiber orientation distributions using high angular resolution diffusion imaging. *Magnetic Resonance in Medicine*, 54:1194–1206, 2005.

[4] A. Anwander, M. Tittgemeyer, D. Y. von Cramon, A. D. Friederici, and T. R. Knosche. Connectivity-based parcellation of broca's area. *Cerebral Cortex*, 17(4):816–825, 2007.

[5] Y. Assaf and P.J. Basser. Composite hindered and restricted model of diffusion (charmed) mr imaging of the human brain. *NeuroImage*, 27(1):48–58, 2005.

[6] P.J. Basser, J. Mattiello, and D. LeBihan. Estimation of the effective self-diffusion tensor from the NMR spin echo. *Journal of Magnetic Resonance*, B(103):247–254, 1994.

[7] P.J. Basser, S. Pajevic, C. Pierpaoli, J. Duda, and A. Aldroubi. In vivo fiber tractography using DT-MRI data. *Magnetic Resonance in Medicine*, 44:625–632, 2000.

[8] T. E. J. Behrens, H. Johansen-Berg, S. Jbabdi, M. F. S. Rushworth, and M. W. Woolrich. Probabilistic diffusion tractography with multiple fibre orientations. what can we gain? *NeuroImage*, 34(1):144–155, 2007.

[9] T.E.J. Behrens, M.W. Woolrich, M. Jenkinson, H. Johansen-Berg, R.G. Nunes, S. Clare, P.M. Matthews, J.M. Brady, and S.M. Smith. Characterization and propagation of uncertainty in Diffusion-Weighted MR Imaging. *Magnetic Resonance in Medicine*, 50:1077–1088, 2003.

[10] J. S. W. Campbell, P. Savadjiev, K. Siddiqi, and B. G. Pike. Validation and regularization in diffusion mri tractography. In *Third IEEE International Symposium on Biomedical Imaging (ISBI): from Nano to Macro*, pages 351–354, Arlington, Virginia, USA, 2006.

[11] J.S.W. Campbell, K. Siddiqi, V.V. Rymar, A. Sadikot, and B.G. Pike. Flow-based fiber tracking with diffusion tensor q-ball data: Validation and comparison to principal diffusion direction techniques. *NeuroImage*, 27(4):725–736, October 2005.

[12] M. Catani, R.J. Howard, S. Pajevic, and D.K. Jones. Virtual in vivo interactive dissection of white matter fasciculi in the human brain. *Neuroimage*, 17:77–94, 2002.

[13] T.E. Conturo, N.F. Lori, T.S. Cull, E. Akbudak, A.Z. Snyder, J.S. Shimony, R.C. McKinstry, H. Burton, and M.E. Raichle. Tracking neuronal fiber pathways in the living human brain. *Proceedings of the National Academy of Sciences*, 96:10422–10427, August 1999.

[14] F. Dell'Acqua, G. Rizzo, P. Scifo, R.A. Clarke, G. Scotti, and F. Fazio. A model-based deconvolution approach to solve fiber crossing in diffusion-weighted mr imaging. *Transactions in Biomedical Engineering*, 54(3):462–472, 2007.

[15] F. Dell'Acqua, P. Scifo, G. Rizzo, G. Scotti, and F. Fazio. An adaptative regularization of richardson lucy spherical deconvolution to reduce isotropic effects. In *15th Scientific Meeting of the ISMRM*, page 1473, Berlin, June 2007.

[16] M. Descoteaux, E. Angelino, S. Fitzgibbons, and R. Deriche. A linear and regularized odf estimation algorithm to recover multiple fibers in q-ball imaging. Technical Report 5768, INRIA Sophia Antipolis, November 2005.

[17] M. Descoteaux, E. Angelino, S. Fitzgibbons, and R. Deriche. Apparent diffusion coefficients from high angular resolution diffusion imaging: Estimation and applications. *Magnetic Resonance in Medicine*, 56:395–410, 2006.

[18] M. Descoteaux, E. Angelino, S. Fitzgibbons, and R. Deriche. Regularized, fast, and robust analytical q-ball imaging. *Magnetic Resonance in Medicine*, 2007, to appear.

[19] Maxime Descoteaux and Rachid Deriche. Sharpening improves clinically feasible q-ball imaging reconstructions. In *Joint Annual Meeting ISMRM-ESMRMB*, Berlin, Germany, 19-25th May 2007, to appear. International Society of Magnetic Resonance in Medicine.

[20] Maxime Descoteaux, Rachid Deriche, and Christophe Lenglet. Diffusion tensor sharpening improves white matter tractography. In *SPIE Medical Imaging*, San Diego, California, USA, Febuary 2007.

[21] O. Friman, G. Farneback, and C.-F. Westin. A bayesion approach for stochastic white matter tractography. *IEEE Transactions in Medical Imaging*, 25(8), 2006.

[22] FSL. Fmrib software library. *University of Oxford*, 2006.

[23] W. Guo, Q. Zeng, Y. Chen, and Y. Liu. Using multiple tensor deflection to reconstruct white matter fiber traces with branching. In *Third IEEE International Symposium on Biomedical Imaging: from Nano to Macro*, pages 69–72, Arlington, Virginia, USA, April 2006.

[24] P. Hagmann, T. G. Reese, W.-Y. I. Tseng, R. Meuli, J.-P. Thiran, and V. J. Wedeen. Diffusion spectrum imaging tractography in complex cerebral white matter: an investigation of the centrum semiovale. In *ISMRM 12th Scientific Meeting and Exhibition*, page 623. International Society for Magnetic Resonance in Medicine, 2004.

[25] Patric Hagmann, Lisa Jonasson, Philippe Maeder, Jean-Philippe Thiran, Van J. Wedeen, and Reto Meuli. Understanding diffusion mr imaging techniques: From scalar diffusion-weighted imaging to diffusion tensor imaging and beyond. *RadioGraphics*, 26:S205–S223, 2006.

[26] C.P. Hess, P. Mukherjee, E.T. Han, D. Xu, and D.B. Vigneron. Q-ball reconstruction of multimodal fiber orientations using the spherical harmonic basis. *Magnetic Resonance in Medicine*, 56:104–117, 2006.

[27] M. Hlawitschka and G. Scheuermann. Hot-lines: Tracking lines in higher order tensor fields. In *IEEE Visualization 2005*, pages 27–34, Los Alamitos, CA, USA, October 2005. IEEE Computer Society.

[28] Sabine Hofer and Jens Frahm. Topography of the human corpus callosum revisited-comprehensive fiber tractography using diffusion tensor magnetic resonance imaging. *NeuroImage*, 32(3):989–994, 2006.

[29] M.A. Horsfield and D. K. Jones. Applications of diffusion-weighted and diffusion tensor mri to white matter diseases - a review. *NMR in Biomedicine*, 15:570–577, 2002.

[30] K. M. Jansons and D. C. Alexander. Persistent angular structure: new insights fom diffusion magnetic resonance imaging data. *Inverse Problems*, 19:1031–1046, 2003.

[31] Mark Jenkinson, Peter Bannister, Michael Brady, and Stephen Smith. Improved optimization for the robust and accurate linear registration and motion correction of brain images. *NeuroImage*, 17(2):825–841, October 2002.

[32] D. K. Jones, M. A. Horsfield, and A. Simmons. Optimal strategies for measuring diffusion in anisotropic systems by magnetic resonance imaging. *Magnetic Resonance in Medicine*, 42:515–525, 1999.

[33] D. K. Jones, S. C. R. Williams, D. Gasston, M. A. Horsfield, A. Simmons, and R. Howard. Isotropic resolution diffusion tensor imaging with whole brain acquisition in a clinically acceptable time. *Human Brain Mapping*, 15:216–230, 2002.

[34] E. Kaden, T. R. Knosche, and A. Anwander. Parametric spherical deconvolution: Inferring multiple fiber bundles using diffusion mr imaging. *NeuroImage*, 37:474–488, 2007.

[35] M.A. Koch, D.G. Norris, and M. Hund-Georgiadis. An investigation of functional and anatomical connectivity using magnetic resonance imaging. *NeuroImage*, 16:241–250, 2002.

[36] B. W. Kreher, J. F. Schneider, J. Mader, E. Martin, Hennig J, and K.A. Il'yasov. Multitensor approach for analysis and tracking of complex fiber configurations. *Magnetic Resonance in Medicine*, 54:1216–1225, 2005.

[37] M. Lazar and A. L. Alexander. Bootstrap white matter tractography (boot-tract). *NeuroImage*, 24:524–532, 2005.

[38] M. Lazar, D.M. Weinstein, J.S. Tsuruda, K.M. Hasan, K. Arfanakis, M.E. Meyerand, B. Badie, H.A. Rowley, V.Haughton, A. Field, and A.L. Alexander. White matter tractography using diffusion tensor deflection. In *Human Brain Mapping*, volume 18, pages 306–321, 2003.

[39] C. Lenglet, M. Rousson, R. Deriche, and 0. Faugeras. Statistics on the manifold of multivariate normal distributions: Theory and application to diffusion tensor mri processing. *Journal of Mathematical Imaging and Vision*, 25(3), 2006.

[40] C. Liu, R. Bammer, B. Acar, and M. E. Moseley. Characterizing non-gaussian diffusion by using generalized diffusion tensors. *Magnetic Resonance in Medicine*, 51:924–937, 2004.

[41] S. Mori, B.J. Crain, V.P. Chacko, and P.C.M. Van Zijl. Three-dimensional tracking of axonal projections in the brain by Magnetic Resonance Imaging. *Annals of Neurology*, 45(2):265–269, February 1999.

[42] S. Mori and P. C. M. van Zijl. Fiber tracking: principles and strategies - a technical review. *NMR in Biomedicine*, 15:468–480, 2002.

[43] E. Ozarslan, T.M. Shepherd, B.C. Vemuri, S.J. Blackband, and T.H. Mareci. Resolution of complex tissue microarchitecture using the diffusion orientation transform (dot). *NeuroImage*, 31(3):1086–1103, 2006.

[44] G. J. M. Parker and D. C. Alexander. Probabilistic anatomical connectivity derived from the microscopic persistent angular structure of cerebral tissue. *Philosophical Transactions of the Royal Society, Series B*, 360:893–902, 2005.

[45] G.J.M. Parker and D.C Alexander. Probabilistic monte carlo based mapping of cerebral connections utilising whole-brain crossing fibre information. In *IPMI*, pages 684–695, 2003.

[46] M. Perrin, C. Poupon, Y. Cointepas, B. Rieul, N. Golestani, C. Pallier, D. Riviere, A. Constantinesco, D. Le Bihan, and J.-F. Mangin. Fiber tracking in q-ball fields using regularized particle trajectories. In *Information Processing in Medical Imaging*, pages 52–63, 2005.

[47] Cyril Poupon, Fabrice Poupon, Lionel Allirol, and Jean-FranÂois Mangin. A database dedicated to anatomo-functional study of human brain connectivity. In *Twelfth Annual Meeting of the Organization for Human Brain Mapping (HBM)*, 2006.

[48] Gary Price, Mara Cercignani, Geoffrey J.M. Parker, Daniel R. Altmann, Thomas R.E. Barnes, Gareth J. Barker, Eileen M. Joyce, and Maria A. Ron. Abnormal brain connectivity in first-episode psychosis: A diffusion mri tractography study of the corpus callosum. *NeuroImage*, 2007, In Press.

[49] A. Ramirez-Manzanares and M. Rivera. Basis tensor decomposition for restoring intra-voxel structure and stochastic walks for inferring brain connectivity in dt-mri. *International Journal of Computer Vision*, 69(1):77 – 92, 2006.

[50] Ken E. Sakaie and Mark J. Lowe. An objective method for regularization of fiber orientation distributions derived from diffusion-weighted mri. *NeuroImage*, 34:169–176, 2007.

[51] P. Savadjiev, J. S. W. Campbell, B. G. Pike, and K. Siddiqi. 3d curve inference for diffusion mri regularization and fibre tractography. *Medical Image Analysis*, 10:799–813, 2006.

[52] Peter Savadjiev, Jennifer Campbell, Maxime Descoteaux, Rachid Deriche, G. B. Pike, and K. Siddiqi. Disambiguation of complex subvoxel fibre configurations in high angular resolution fibre tractography. In *15th Scientific Meeting of the ISMRM*, page 1477, Berlin, 2007.

[53] Jean Talairach and Pierre Tournoux. *Co-Planar Stereotaxic Atlas of the Human Brain: 3-Dimensional Proportional System : An Approach to Cerebral Imaging*. Thieme Medical Publishers, January 1988.

[54] J.-D. Tournier, F. Calamante, D.G. Gadian, and A. Connelly. Diffusion-weighted magnetic resonance imaging fibre tracking using a front evolution algorithm. *NeuroImage*, 20:276–288, 2003.

[55] J.-D. Tournier, F. Calamante, D.G. Gadian, and A. Connelly. Direct estimation of the fiber orientation density function from diffusion-weighted mri data using spherical deconvolution. *NeuroImage*, 23:1176–1185, 2004.

[56] J-Donald Tournier, Fernando Calamante, and Alan Connelly. Robust determination of the fibre orientation distribution in diffusion mri: Non-negativity constrained super-resolved spherical deconvolution. *NeuroImage*, 35(4):1459–1472, 2007.

[57] D. Tuch. *Diffusion MRI of Complex Tissue Structure*. PhD thesis, Harvard University and Massachusetts Institute of Technology, 2002.

[58] D. Tuch. Q-ball imaging. *Magnetic Resonance in Medicine*, 52(6):1358–1372, 2004.

[59] C.F. Westin, S.E. Maier, H. Mamata, A. Nabavi, F.A. Jolesz, and R. Kikinis. Processing and visualization for diffusion tensor mri. *Medical Image Analysis*, 6(2):93–108, June 2002.

Unité de recherche INRIA Sophia Antipolis
2004, route des Lucioles - BP 93 - 06902 Sophia Antipolis Cedex (France)

Unité de recherche INRIA Futurs : Parc Club Orsay Université - ZAC des Vignes
4, rue Jacques Monod - 91893 ORSAY Cedex (France)
Unité de recherche INRIA Lorraine : LORIA, Technopôle de Nancy-Brabois - Campus scientifi que
615, rue du Jardin Botanique - BP 101 - 54602 Villers-lès-Nancy Cedex (France)
Unité de recherche INRIA Rennes : IRISA, Campus universitaire de Beaulieu - 35042 Rennes Cedex (France)
Unité de recherche INRIA Rhône-Alpes : 655, avenue de l'Europe - 38334 Montbonnot Saint-Ismier (France)
Unité de recherche INRIA Rocquencourt : Domaine de Voluceau - Rocquencourt - BP 105 - 78153 Le Chesnay Cedex (France)

Éditeur
INRIA - Domaine de Voluceau - Rocquencourt, BP 105 - 78153 Le Chesnay Cedex (France)
http://www.inria.fr
ISSN 0249-6399